TECHNISCHE UNIVERSITÄT WIEN
Vienna University of Technology

DIPLOMARBEIT

A transportable polarization-entangled photon source

Ausgeführt am

Atominstitut

der Technischen Universität Wien

unter der Anleitung von

o.Univ.-Prof. Dr. Anton Zeilinger

durch

Johannes Handsteiner

Wachtberg 17, 3365 Allhartsberg

December 2014

Johannes Handsteiner

TECHNISCHE UNIVERSITÄT WIEN

Abstract

Fakultät für Physik
Atominstitut

Master of Science

A transportable polarization-entangled photon source

by Johannes Handsteiner

Within the quantum experiments at space scale project, we want to distribute a quantum key between a satellite and optical ground stations. A mobile polarization-entangled photon source would be useful to pretest the optical ground stations before the satellite is in orbit. Within this thesis I describe the successful approach of building this transportable entangled photon source.

Contents

Chapter 1

Introduction

Quantum physics is nowadays one of the main areas of modern physics. It has been well tested at length scales and velocities available in ground based laboratories. Quantum mechanics still leads to interesting and counterintuitive situations such as wave-particle duality or quantum entanglement. The interpretation of quantum physics is still an ongoing discussion involving the role of reality and locality in nature. Furthermore, the theory behind quantum mechanics requires interpretations of nature that are contradictory to those of our classical world and every-day experiences. This knowledge merges nowadays together with the information and computational science to the novel field of quantum information science. Within this thesis I will focus on the concepts of quantum cryptography as part of this science, providing new concepts which are much more powerful compared to the classical cryptography. Additionally, I will investigate fundamental test of nature based on photonic entanglement

An application of quantum cryptography is quantum key distribution(QKD). This was suggested by Bennet and G. Brassard [1] in 1984 for the first time. With QKD, an unconditionally secure key can be generated between two communicating parties. Therefore, they are able to exchange messages/data tap-proof. Today such systems are more relevant than ever. In order to put quantum communication on a global scale there is no way around going into space. This is because ground based free-space communications links are limited either by the curvature of the earth and fibre links are limited by the attenuation within the optical fibre. Moreover, the unique space environment offers the potential for performing quantum experiments beyond distances and velocities achievable on ground where effects of quantum physics and relativity begin to interplay.

Within the Quantum Experiments at Space Scale (QUESS) project we want to establish a satellite to ground link for QKD. This project is a collaboration between the Chinese

Academy of Science(CAS) and the Austrian Academy of Science(AAS). The CAS will launch a dedicated quantum science satellite with a faint laser pulse source for demonstrating decoy state QKD in a downlink scenario. Based on a cooperation contract, our institute was invited to be part of these experiments providing four optical ground stations in Europe to receive the signal from the satellite. Those stations are located in Vienna, Graz, Kephalonia and Tenerife. In order to pretest the receiving telescopes and its components whether they are capable for detecting and computing the incoming photons, two different mobile single photon sources should be used. The first one is a decoy source with similar characteristics as the source on the satellite. This source produces faint laser pulses with a certain polarization and is currently being developed within a project funded by the European Space Agency(ESA) together with the Institute of Photonic Sciences(ICFO) in Barcelona. The second source is an polarization-entangled photon source which should be transportable, such that it can easily be set up at the different ground stations. In the main part of this thesis I will describe my approach to build such a highly mobile entangled photon source. Additionally, I will describe further components which are important for the QUESS project.

Chapter 2

Theory

Within this chapter I want to give a brief overview of important concepts of quantum theory, which are relevant for this work.

2.1 Qubits

A classical bit can either be "0" or "1". A quantum bit(qubit) can exist in a superposition of the states $|0\rangle$ and $|1\rangle$ and is the quantum mechanical analog to the classical bit. It can be realized by any two-level quantum system, and its state is represented by

$$|\Psi\rangle = \alpha |0\rangle + \beta |1\rangle \text{ with } |\alpha|^2 + |\beta|^2 = 1 \tag{2.1}$$

Equation 2.1 does not mean that the value of the qubit is somewhere between "0" and "1" but the outcome of the measurement will be "0" or "1" with a probability of $|\alpha|^2$ or $|\beta|^2$, respectively. In the experiments considered in this work, the qubit is realized with two orthogonal polarization states of a single photon, with horizontal polarization corresponding to $|0\rangle$ and vertical to $|1\rangle$, respectively. This polarization-encoded qubit can be visualized on the Poincarê sphere(shown in fig.2.1), where Φ and Θ denote the azimuth and zenith angles:

$$|\Psi\rangle = cos\left(\frac{\Theta}{2}\right)|H\rangle + e^{i\Phi} sin\left(\frac{\Theta}{2}\right)|V\rangle \tag{2.2}$$

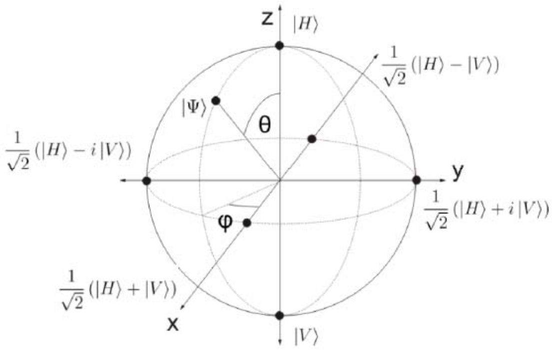

FIGURE 2.1: The representation of the polarization-encoded qubit on the Poincarê sphere (see Eq. 2.2)(Figure taken from [2]).

Listed below are the most important polarization states of a photonic qubit. Any polarization state can be expressed via a linear combination of $|H\rangle$ and $|V\rangle$ polarization.

polarization state	linear combination	named	linear polarization angle
$\|H\rangle$	$\|H\rangle$	horizontal	0°
$\|V\rangle$	$\|V\rangle$	vertical	90°
$\|D\rangle$	$\frac{1}{\sqrt{2}}(\|H\rangle + \|V\rangle)$	diagonal	45°
$\|A\rangle$	$\frac{1}{\sqrt{2}}(\|H\rangle - \|V\rangle)$	anti-diagonal	135°
$\|R\rangle$	$\frac{1}{\sqrt{2}}(\|H\rangle + i\,\|V\rangle)$	right-handed circular	-
$\|L\rangle$	$\frac{1}{\sqrt{2}}(\|H\rangle - i\,\|V\rangle)$	left-handed circular	-

TABLE 2.1: Table of the most important polarization states of a photonic qubit. Any polarization state can be expressed as a linear combination of horizontal and vertical polarization.

2.1.1 The no-cloning theorem

In quantum mechanics, it is not possible to copy nor to amplify an arbitrary unknown quantum state of a qubit onto a different qubit, without disturbing the quantum state of the original qubit. This is called the no-cloning theorem[3]. In order to show that such a perfect cloning machine can not exist we assume a device, which copies an input qubit i onto a blank qubit o as follows

$$\begin{aligned} |0\rangle_i\,|0\rangle_o &\rightarrow |0\rangle_i\,|0\rangle_o \\ |1\rangle_i\,|0\rangle_o &\rightarrow |1\rangle_i\,|1\rangle_o \end{aligned} \tag{2.3}$$

Contrary to a classical bit, the input bit can be in the superposition state $\frac{1}{\sqrt{2}}(|0\rangle_i + |1\rangle_i)$ and together with the linearity of quantum mechanics this results in

$$\frac{1}{\sqrt{2}}(|0\rangle_i + |1\rangle_i)\,|0\rangle_o \rightarrow \frac{1}{\sqrt{2}}(|0\rangle_i\,|0\rangle_o + |1\rangle_i\,|1\rangle_o) \tag{2.4}$$

where the output state is an entangled state and obviously different from the desired copy of the input state

$$\begin{aligned}\frac{1}{\sqrt{2}}(|0\rangle_i + |1\rangle_i)\,|0\rangle_o \rightarrow \frac{1}{\sqrt{2}}(|0\rangle_i + |1\rangle_i)\frac{1}{\sqrt{2}}(|0\rangle_o + |1\rangle_o))\\ = \frac{1}{\sqrt{2}}(|0\rangle_i\,|0\rangle_o + |0\rangle_i\,|1\rangle_o + |1\rangle_i\,|0\rangle_o + |1\rangle_i\,|1\rangle_o).\end{aligned} \tag{2.5}$$

This proves that a deterministic quantum cloning device cannot exist, although there exist probabilistic cloning strategies[4] which can achieve a successful cloning probability of $\frac{5}{6}$.

2.2 Bell states

A composite quantum system is described in a Hilbert space, which is given by the tensor product of its n subsystem spaces

$$\mathcal{H} = \bigotimes_{i=1}^{N} \mathcal{H}_i \tag{2.6}$$

In the case of $N = 2$ and considering polarization encoded qubits the states in Eq. 2.7 form a orthonormal basis of the corresponding four-dimensional Hilbert space. These states are called Bell states. They cannot be written as a tensor product of their subsystem states, therefore they are not separable. Such non-separable states are called entangled. Bell states are maximally entangled quantum states and they have interesting properties. The outcome of a measurement on one qubit is random, but the outcome of the other qubit is perfectly (anti-)correlated in theory. The strength of the correlations do not depend on the distance between the subsystems, which is called quantum non-locality.

$$
\begin{aligned}
|\psi^-\rangle_{12} &= \frac{1}{\sqrt{2}})\,|H\rangle_1\,|V\rangle_2 - |V\rangle_1\,|H\rangle_2) \\
|\psi^+\rangle_{12} &= \frac{1}{\sqrt{2}})\,|H\rangle_1\,|V\rangle_2 + |V\rangle_1\,|H\rangle_2) \\
|\phi^-\rangle_{12} &= \frac{1}{\sqrt{2}})\,|H\rangle_1\,|H\rangle_2 - |V\rangle_1\,|V\rangle_2) \\
|\phi^+\rangle_{12} &= \frac{1}{\sqrt{2}})\,|H\rangle_1\,|H\rangle_2 + |V\rangle_1\,|V\rangle_2)
\end{aligned}
\tag{2.7}
$$

In most of the experiments described in this work the $|\psi^-\rangle$ state in Eq. 2.7 is used. It is a rotation-invariant state and therefore polarization is anti-correlated in every measurement basis.

$$
|\psi^-\rangle_{12} = \frac{1}{\sqrt{2}}(|H\rangle_1\,|V\rangle_2 - |V\rangle_1\,|H\rangle_2) = \frac{1}{\sqrt{2}}(|D\rangle_1\,|A\rangle_2 - |A\rangle_1\,|D\rangle_2) = \frac{1}{\sqrt{2}}(|R\rangle_1\,|L\rangle_2 - |L\rangle_1\,|R\rangle_2)
\tag{2.8}
$$

2.3 EPR paradox

In their paper [5] A. Einstein, B. Podolsky and N. Rosen(EPR) discussed in 1935 the fascinating implications of entanglement. They made three vital assumptions about a physical theory:

completeness: A physical theory is complete , if there is for every element in reality a counterpart in the physical theory.
reality: If you can predict a physical property with probability of one, then there is an element of physical reality that corresponds to this quantity.
locality: If there are two space like separate systems, such that they can not interact with each other, a measurement on one system can not have an effect on the other.

These criteria can be used to define a whole class of physical theories, which is today known as the class of local-hidden-variable theories.
Based on a thought experiment Einstein, Podolsky and Rosen showed that in a system of two position-momentum entangled particles, a measurement on particle 1 determines the state of particle 2 without disturbing it, even if the two particles are space-like separated. For example if you measure the position of particle 1 so the position of particle 2 is determined. According to the reality criteria the position of particle 2 is also an element of reality. This is also valid for the momentum. Hence, one could without affecting particle 2 predict two eigenvalues from two non commuting operators. This is not

allowed in quantum theory. The conclusion of EPR was that quantum theory cannot describe reality completely. Therefore one might need so called local hidden variables to complete the theory. Hidden variables would contain all properties of the system, but would appear only as probability distribution in quantum theory.

In 1957, David Bohm revised the EPR thought experiment[6]. Instead of using position and momentum entangled particles he considered spin-$\frac{1}{2}$ particles. However, although he considered spin-$\frac{1}{2}$ particles, I will consider polarization entangled photons, since all experiments described in this thesis are using these quantum systems. Suppose we have two photons in the maximally entangled state $|\psi^-\rangle$ (shown in Eq. 2.8) and they are widely separated. Due to the rotation invariance, an observer can now choose to measure photon 1 in any of two complementary bases. If photon 2 is measured in the same basis it is with certainty in the orthogonal state. So the outcome of the measurement on photon 2 is predictable without actually disturbing/measuring it. According to EPR again, these complementary states for photon 2 must be simultaneous elements of reality. This is in contradiction with quantum mechanics, because, if the outcome of a measurement in a basis is certain the results of a measurement in the complementary basis will be random. According to quantum mechanics, two complementary states can never be simultaneous elements of reality.

2.4 Bell- and CHSH inequality

For many years these EPR thought experiments founded philosophical debates until John Bell showed 1964 in his paper "On the Einstein Podolsky Rosen Paradox" [7] the inconsistency of predictions made by any local realistic theories and quantum mechanics. He formulated an inequality which gives a boundary for those local realistic theories. However, Bell assumed perfect correlations and a detection efficiency of 100%, which is not applicable for realistic experiments. In 1969 Clauser, Horne, Shimony and Holt(CHSH) [8] modified the Bell inequality and better adapted it to the experimental constraints. It supposes that the detectors and the entangled states do not need to be perfect any more. The CHSH inequality is defined by

$$S := |P(\vec{a},\vec{b}) - P(\vec{a},\vec{b}')| + |P(\vec{a}',\vec{b}') + P(\vec{a}',\vec{b})| \leq 2. \tag{2.9}$$

If we now restrict our unit vectors (in Eq. 2.9) to lie in one plane in the three dimensional space, we can substitute them with the corresponding angles $\alpha, \beta, \alpha', \beta'$. With the "Bell test angles" $\alpha = 0°$, $\beta = 22.5°$, $\alpha' = 45°$ and $\beta' = 67.5°$ quantum mechanics predicts the strongest violation with $S^{qt}_{max} = 2\sqrt{2} \sim 2.83 \nleq 2 = S^{cl}_{max}$, where S^{cl}_{max} denotes the classical boundary for local realistic theories and S^{qt}_{max} the boundary of quantum theory, respectively. The expectation function P is

$$P_{(\alpha,\beta)} = \frac{N_k(\alpha,\beta) - N_k(\alpha,\beta^{\perp}) - N_k(\alpha^{\perp},\beta) + N_k(\alpha^{\perp},\beta^{\perp})}{N_k(\alpha,\beta) + N_k(\alpha,\beta^{\perp}) + N_k(\alpha^{\perp},\beta) + N_k(\alpha^{\perp},\beta^{\perp})} \tag{2.10}$$

where N_k is the coincidence detection rate at the associated measurement angles($\alpha, \beta, \alpha^{\perp}, \beta^{\perp}$).

The variance of S is calculated as following Gaussian error propagation as:

$$\Delta S = \sqrt{(\Delta P(\alpha,\beta)^2 + (\Delta P(\alpha,\beta')^2)) + (\Delta P(\alpha',\beta)^2) + (\Delta P(\alpha',\beta')^2)}, \tag{2.11}$$

with

$$\Delta P = \sqrt{\frac{1}{N}(1 - P^2)}. \tag{2.12}$$

The full derivation of the error propagation is shown appendix A.2.

2.5 QKD protocols

Quantum cryptography harnesses quantum mechanical effects to carry out cryptographic tasks or to break classical cryptographic systems. Quantum key distribution(QKD) is a well known example of quantum cryptography. With QKD two parties can exchange a secret random key to encrypt and decrypt messages. This key is unconditional secure if it is completely random, used only once and at least as long as the plain-text. One party encrypts the message with this key. Afterwards, this message can be sent over a classical channel(e.g. the internet) and the second party decrypts again with the same key. Two QKD protocols are subsequently explained, which are relevant for this work.

2.5.1 BB84 protocol

1984 C.H. Bennett and G. Brassard developed the BB84 protocol [1]. It utilizes four polarization states from two mutually unbiased basis($|H\rangle, |V\rangle, |D\rangle, |A\rangle$). Typically $|H\rangle$ and $|D\rangle$ are assigned with the binary value 1 and $|V\rangle$ and $|A\rangle$ with 0. The two bases are maximal complementary meaning that:

$$\langle H|D\rangle = \langle V|A\rangle = \langle V|D\rangle = \langle H|A\rangle = \frac{1}{\sqrt{2}} \tag{2.13}$$

$$\langle V|H\rangle = \langle A|D\rangle = 0 \tag{2.14}$$

The concept of the BB84 protocol is depicted in Fig.2.2. Alice sends single photons randomly in one of the four polarization states. Bob measures the photons also randomly in one of the two basis ($|H\rangle / |V\rangle \, or \, |D\rangle / |A\rangle$) and saves the binary value. This string of bits is the so called raw key. In 50% of the cases Alice and Bob agree with the basis and in the other 50% the bases do not match. Hence, the raw key has an error rate of 25% (according to Eq. 2.13). Afterwards Bob compares with Alice in which basis every qubit was prepared/measured. This is called basis reconciliation. This can be done over a classical channel because the measurement basis without the measurement result carries no information. Only qubits which were measured in the proper basis are part of the so called sifted key.

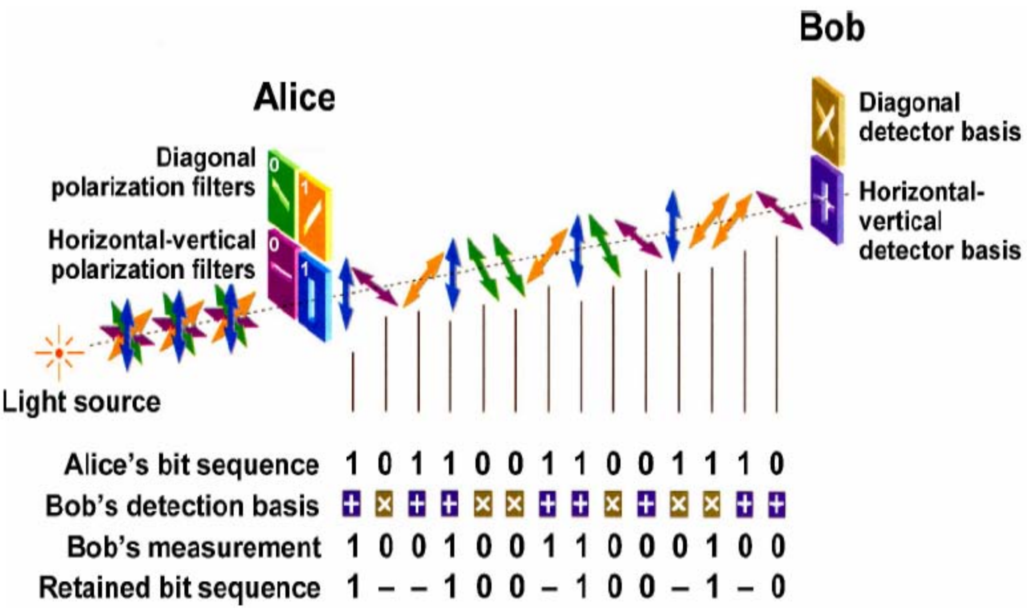

FIGURE 2.2: Scheme of the BB84 protocol (Figure taken from [9]). Alice prepares and sends single photons randomly in one of the four polarization states. Bob measures the photons randomly either in $|H\rangle / |V\rangle \, or \, |D\rangle / |A\rangle$ measurement basis. Only photons measured in the correct basis contribute to the key.

Security

Let us assume that an eavesdropper(Eve) is intercepting part of the key. Therefore Bob is not detecting these qubits. This leads only to a reduction of the received bit sequence but does not compromise the security. A more sophisticated strategy is the so called intercept-resend strategy. Eve measures the qubit and resends a copy. According to the no-cloning theorem (explained in chapter 2.3) such a copying device cannot exist. Therefore Eve gains only 50% of the information from the key and introduces a quantum bit error rate(QBER) of 25% into the sifted key. Through comparison of a subset of the key, an eavesdropper can be easily detected. If Eve is only intercepting 10% of the photons then the introduced QBER in the sifted key is only 2.5% whereas the gained information is 5%. Due to noise and an imperfect experimental setup the sifted key already contains errors, therefore it is harder to detect an eavesdropper. In order to counteract such attacks, classical error correction and privacy amplification can be used. The error correction compares the parity of subsets of the sifted key in order to correct wrong bits. To further erase the information a potential eavesdropper might gain during the error correction process the procedure named privacy amplification has to be applied. This result in a secure error-free key which is shorter than the sifted key. Shor and Preskill derived a lower bound for the maximal QBER in their security proof[10] by considering arbitrary eavesdropping attacks possible within the laws of quantum mechanics. Regarding to the BB84 protocol they showed that, a secure key rate (SKR), depending on the quantum bit error rate of at least

$$SKR(q) = 1 - 2H_2(q) \tag{2.15}$$

can be extracted out of the sifted key. Here q denotes the QBER in the sifted key and the binary Shannon Entropy $H_2(q)$ is given with

$$H_2(q) = -q log_2(q) - (1-q) log_2(1-q). \tag{2.16}$$

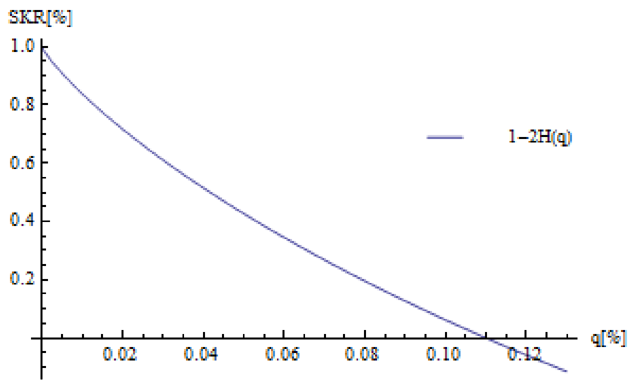

Figure 2.3: The calculated plot of the secure key rate(SKR), which can be distilled out of a defective sifted key, depending on the quantum bit error rate q.

If the quantum bit error rate is higher than $\sim 11\%$ no secure key can be extracted any more. A disadvantage of this protocol is that Bob can not prove if Alice itself is corrupted(in Eve's hand) and therefore Alice must be trusted.

The assumed single photon source gives in practise rise to another security attack. Alice sends in the ideal case single photons, but in the experiment usually attenuated faint laser pulses are used, emitting light according to a Poisson photo number distribution.

The probability of finding n photons in such an faint laser pulse is given by

$$P(n,\mu) = \frac{\mu^n}{n!}e^{-\mu}, \tag{2.17}$$

where μ denotes the mean photon number per pulse. Eve could block all pulses where only one photon was sent. Whenever a signal pulse contains more than one photon, Eve splits one photon off and forwards the remaining photons to Bob. Eve keeps the photons until Alice and Bob communicate their measurement basis, and performs the measurement in the correct basis afterwards. To counteract this photon number split(PNS) attack, decoy pulses can be utilized. These are pulses with a different mean photon number added randomly to the signal pulses. Eve can not distinguish between signal and decoy pulses, to act differently on them and hence introduces different channel loss for the decoy and signal pulses. Alice and Bob can then compute the transmission probability for decoy and signal states and detect a PNS attack.

2.5.2 Entanglement based BB84 protocol

The entanglement based BB84 protocol uses polarization entangled photons instead of weak laser pulses. The photon pairs are prepared e.g. in a $|\psi^-\rangle$ state and distributed to Alice and Bob. Both measure the photons randomly in either the $|H\rangle/|V\rangle$ or the $|D\rangle/|A\rangle$ polarization basis. Since the shared $|\psi^-\rangle$ state is an anti-symmetric state in polarization, Alice's and Bob's results are perfectly anti-correlated when measured in the same basis. As in the BB84 protocol only photons measured in the same basis contribute to the sifted key. After exchanging a key, one of them inverts the bits, and therefore they obtain an identical set of "0"s and "1"s - the sifted key. One of the first demonstrations of entanglement based QKD in a real-world scenario is shown in figure 2.4. In this experiment from A.Poppe et al. [11], they successfully distributed a quantum key with an entangled photon source. One photon was measured next to the source at Alice at the headquarters of the Bank Austria Credit Anstalt. The other photon was sent via optical fibres to Bob, which was located at the Vienna City Hall.

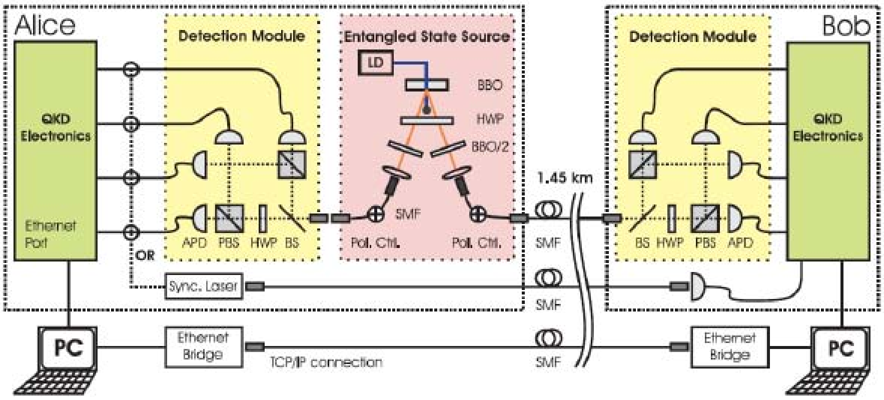

FIGURE 2.4: Setup of the QKD experiment based on entangled photons conducted by A.Poppe et al.(Figure taken from [11]). A source produced polarization-entangled photon pairs which then were distributed via fibres and measured in two detection modules.

Security

The same security constraints apply as for the standard BB84 protocol(explained in chapter 2.5.1). The main advantage of the entanglement based BB84 is that the photon source must not be trusted, which is a consequence of entanglement.

2.6 Spontaneous parametric down conversion

Spontaneous parametric down conversion (SPDC) is a second-order non-linear process in a crystal and it is a common method to create entangled photon pairs[12]. Thereby, a high energy pump photon creates a pair of photons (called signal and idler) under energy and momentum conservation. We distinguish between type-I and type-II SPDC depending on whether the produced photons have the same or orthogonal polarization. In an experiment usually an ultra violet pump laser with a wavelength of $405nm$ is used to produce two collinear orthogonally polarized degenerate infra-red photons at $810nm$. The crystals used in non-linear optics are highly anisotropic and their response to the pump field can be described in tensorial form according to

$$\hat{P}_i(t) = \chi^{(1)}_{ij}\hat{E}_j + \chi^{(2)}_{ijk}\hat{E}_j\hat{E}_k + \chi^{(3)}_{ijkl}\hat{E}_j\hat{E}_k\hat{E}_l + \cdots \tag{2.18}$$

where χ^m denotes the mth-order electric susceptibility tensor [13] and repeated indices imply a sum. The energy density is $\epsilon_0 E_i P_i$ and therefore the second-order contribution to the Hamiltonian, the interaction Hamiltonian, is

$$\hat{H}^{(2)} = \epsilon_0 \int_V d^3\mathbf{r}\chi^{(2)}_{ijk}\hat{E}_k\hat{E}_l, \tag{2.19}$$

where the integral is over the interaction volume. The components of the electric field can be represented as Fourier integrals in the following form

$$\hat{E}(\mathbf{r},t) = \int d^3\mathbf{k}\left[\hat{E}^{(-)}(\mathbf{k})e^{-i[\omega(\mathbf{k})t-\mathbf{k}\cdot\mathbf{r}]} + \hat{E}^{(+)}(\mathbf{k})e^{i[\omega(\mathbf{k})t-\mathbf{k}\cdot\mathbf{r}]}\right] \tag{2.20}$$

where

$$\hat{E}^{(-)}\mathbf{k} = i\sqrt{\frac{2\pi\hbar(\mathbf{k})}{V}}\hat{a}^\dagger(\mathbf{k}) \tag{2.21}$$

and

$$\hat{E}^{(+)}\mathbf{k} = i\sqrt{\frac{2\pi\hbar(\mathbf{k})}{V}}\hat{a}(\mathbf{k}). \tag{2.22}$$

In equation 2.21 and 2.22 $\hat{a}^\dagger(\mathbf{k})$ and $\hat{a}(\mathbf{k})$ are the creation and annihilation operators of the photons with momentum $\hbar\mathbf{k}$, respectively. If we substitute the fields in Eq. 2.21 with the expression in Eq. 2.20 and retain only the terms important when the signal and idler modes are in vacuum states initially, the interaction Hamiltonian looks like

$$\hat{H}_I(t) = \int_V d^3\mathbf{r}\int d^3\mathbf{k}_s d^3\mathbf{k}_i\chi^{(2)}_{lmn}\times\hat{E}^{(+)}_{pl}e^{i[\omega_p(\mathbf{k}_p)t-\mathbf{k}_p\cdot\mathbf{r}]}\hat{E}^{(-)}_{sm}e^{i[\omega_s(\mathbf{k}_s)t-\mathbf{k}_s\cdot\mathbf{r}]}\hat{E}^{(-)}_{in}e^{i[\omega_i(\mathbf{k}_i)t-\mathbf{k}_i\cdot\mathbf{r}]}+H.c. \tag{2.23}$$

The second order electric susceptibility $\chi^{(2)}$ is controlling the conversion rates and typically is in the range between 10^{-7} to 10^{-11}. In order to get a significant output at the signal and idler modes, it is necessary to pump the medium with a very strong coherent field. This field can be seen as a classical field and the photons missing after down conversion may be neglected. This is known as the undepleted classical pump approximation. Assuming the signal and idler modes are initially in vacuum states $|\Psi_0\rangle$ we obtain, to first order, $|\Psi\rangle \sim |\Psi_0\rangle + |\Psi_1\rangle$ where

$$\begin{aligned}|\Psi_1\rangle &= -\frac{i}{\hbar}\int dt\hat{H}(t)\,|\Psi_0\rangle\\ &= \mathcal{N}\int d^3\mathbf{k}_s d^3\mathbf{k}_i\delta(\omega_p-\omega_s(\mathbf{k}_s))-\omega_i(\mathbf{k}_i)\times\delta^{(3)}(\mathbf{k}_p-\mathbf{k}_s-\mathbf{k}_i)\hat{a}^\dagger_s(\mathbf{k}_s)\hat{a}^\dagger_i(\mathbf{k}_i)\,|\Psi\rangle_0\,,\end{aligned} \tag{2.24}$$

where all constants have been absorbed by the normalization factor $\mathcal{N}$. One can see that the delta functions contain the so-called phase matching conditions:

$$\begin{aligned}\omega_p &= \omega_s + \omega_i\\ \mathbf{k}_p &= \mathbf{k}_s + \mathbf{k}_i.\end{aligned} \tag{2.25}$$

2.6.1 Critical and non critical phase matching

In order to achieve efficient SPDC, phase matching between the interacting waves is required. This has been done in non-linear materials through birefringence phase matching. With this technique one has to place the crystal axis to a specific angle to achieve phase matching conditions for a specific wavelength. This technique is very sensitive to the orientation angle of the crystal and therefore it is called critical phase matching. With critical phase matching the angle of emission is set by the angle of the phase-matching condition and results usually in a non collinear emission(shown in Fig. 2.5). More recent schemes use non critical quasi phase matching. The relative phase is corrected at regular intervals using a built in structural periodicity in a non linear crystal(shown in Fig. 2.6). This is called periodic poling. In contrast to birefringent phase matching the quasi phase matching conditions now involve an additional term, which depends on the crystal poling period Λ.

$$\mathbf{k}_p = \mathbf{k}_s + \mathbf{k}_i + \frac{2\pi}{\Lambda} \tag{2.26}$$

In the experimental setup the quasi-phase matching is achieved by choosing the proper crystal polling period Λ and fine-tune the phase matching by changing the temperature of the crystal. The advantage of quasi phase matching is that it is easy to design that signal and idler are collinear. This is crucial for the setup of the entangled photon source we have chosen, because it allows to couple the signal and idler beam into the same fibre optics.

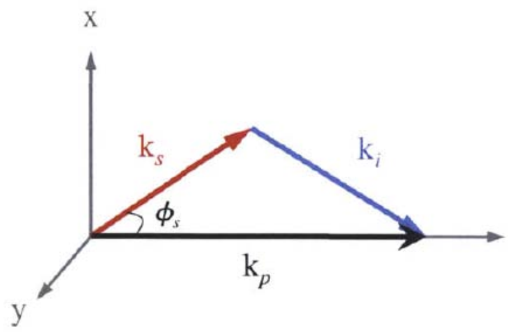

FIGURE 2.5: Illustration of the geometry of noncollinear propagation of pump $\mathbf{k}_p$, signal $\mathbf{k}_s$ and idler $\mathbf{k}_i$ with signal beam emitted under the angle Φ_s(Figure taken from[14]).

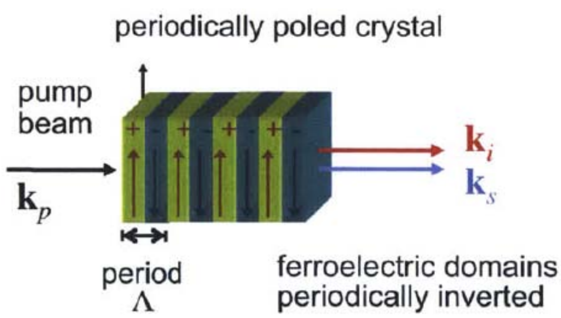

FIGURE 2.6: Illustration of a periodically poled crystal composed of evenly spaced domains with alternating polarization and polling period Λ(Figure taken from[14]).

The effect of no phase matching at all, critical and non-critcal phase matching on the intensity of the SPDC photons is shown in the following graph.

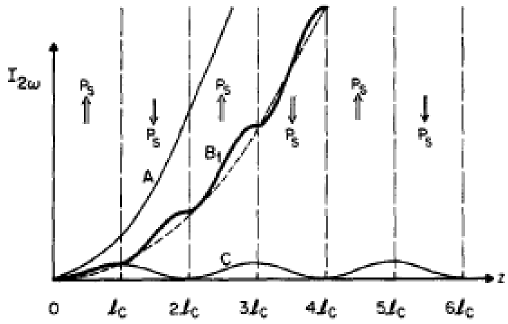

FIGURE 2.7: Effect of phase matching on the growth of second harmonic intensity with distance in a nonlinear crystal. A: perfect phase matching in a unniformly poled crystal; C: nonphase-matched interaction; B1: first-order QPM by flipping the sign of spontaneous polarization every coherence length of the interaction of curve C.(Figure taken from[15])

2.7 Single photon detection

The amount of energy in a single photon is small (e.g. for a 810nm photon $E = \frac{hc}{\lambda} = 2.452 \cdot 10^{-19}J = 1.531eV$)). For example a 100W light bulb emits $2 * 10^{20}$ photons only in the visible range per second. The most efficient single photon detection to date are superconducting transition edge bolometer with a detection efficiency up to 99% and higher. However, this is only achieved with a large technical effort(e.g. cooling the superconductor to the millikelvin regime). The choice of the detection method always depends on the requirement. Suitable for my experiment and mostly common are single-photon avalanche photo diodes(SPADs or APDs).

APDs are semiconductors. They exploit the inner photoelectric effect to produce electron-hole pairs. For that reason the impinging photon needs a higher energy than the band gap between conduction and valence band. For silicon this band gap is $E_g = 1.12eV$ so the cut off wavelength is $\lambda_c = \frac{hc}{E_g} = 1100nm$. For longer wavelength the diode gets transparent. The diode has a $p^+ - i - n^+$ doping profile. This leads to a high space charge and therefore a high electric field as seen in figure 2.8. This zone is called multiplication zone. The weak doped intrisic layer acts as adsorption layer. If a photon produces a electron-hole pair the electron gets due to the high electric field accelerated to the multiplication zone and produces through impact ionization secondary charge carriers. They produce then again more charge carriers like an avalanche (shown in Fig. 2.9).

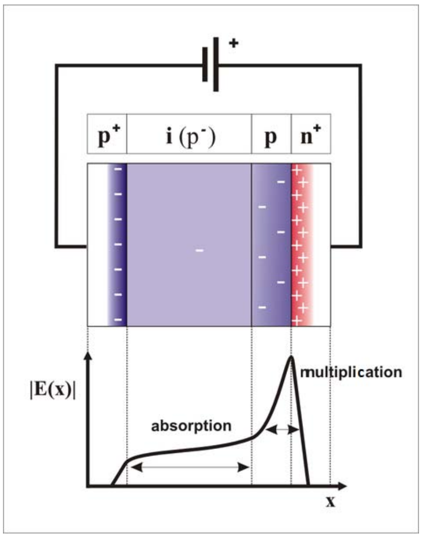

FIGURE 2.8: The scheme illustrates the layer construction of a Si-APD where a reverse voltage is applied. The colour gradient shows the space charge distribution, the graph the corresponding electric field strength(Modified from [16]).

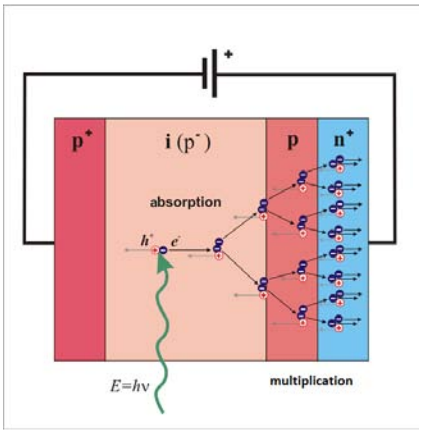

FIGURE 2.9: The scheme of the charge carriers avalanche due to impact ionization when a photon gets absorpted in the charge carrier free absorption zone(Modified from [16]).

For single photon detection APDs are operated in the Geiger mode. In this mode the reverse-bias voltage is well above the breakdown voltage. A photoelectron or also a thermally generated one is able to trigger an avalanche pulse(with 10^8 carriers) which discharges the diode from the reverse voltage to a voltage slightly below the breakdown voltage. The probability for triggering this avalanche is shown in figure 2.11 and it increases with rising reverse voltage. For the overall detection efficiency the photoelectron detection efficiency has to be multiplied with the quantum efficiency and is in our case approximately 50%. Both are relatively temperature independent. The reason for cooling the diode is the exponential reduction of dark counts(shown in Fig. 2.12).

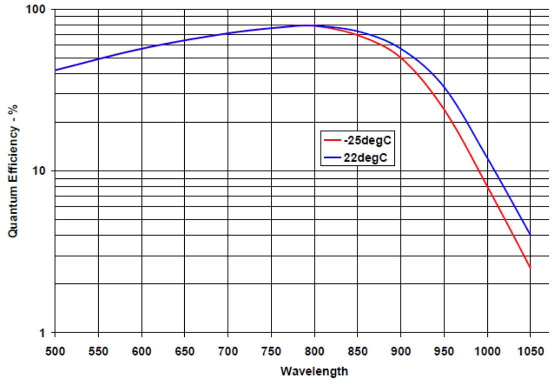

FIGURE 2.10: The calculated graph of the typical quantum efficiency vs. wavelength for two different diode temperatures (Figure from [17]).

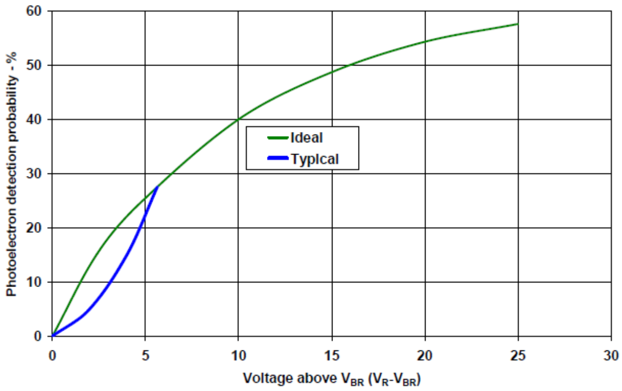

FIGURE 2.11: Geiger mode photon detection probability vs. voltage above V_{BR} at $22°C$ (Figure from [17]).

In order to quench the breakdown pulse there are two possibilities (passive or active quenching). The APD stays in a conducting state until the current I is below the latching current I_{LATCH}. The simplest method is to use a current limiting load resistor(shown in Fig. 2.13). This is called passive quenching. The probability to detect a photon until the diode is recharged is relatively low. In order to avoid this dead time an active quenched circuit is useful. This circuit drops the bias voltage after a photon detection allowing all the charge carriers to recombine. There are now no more electrons in the depletion region to trigger another avalanche or latch the diode after the higher voltage is reapplied. A smaller load resistor can be used and this results in a very rapid recharging. Count rates up to $10MHz$ are achievable compared to less than $1MHz$ witch passive quenched diodes.

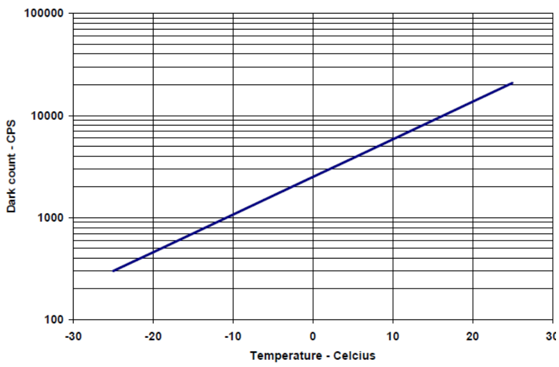

FIGURE 2.12: The calulated graph of typical dark counts vs temperature(Figure from [17]).

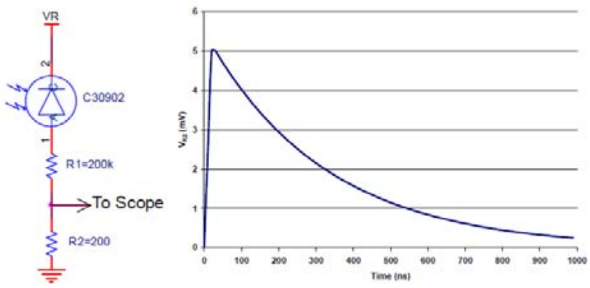

FIGURE 2.13: Sample of a passive quench circuit(Figure from [17]).

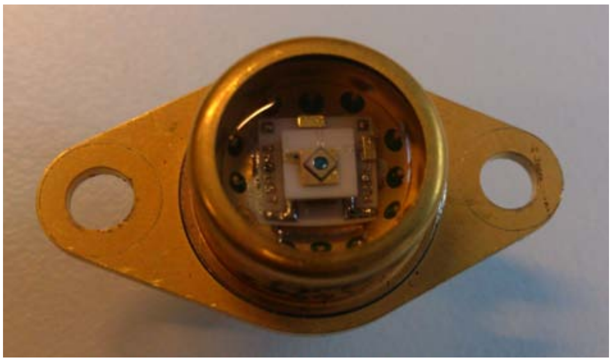

FIGURE 2.14: Image of the C3092SH-DTC avalanche photodiode. The active area in the middle has a diameter of $500\mu m$. The diode is mounted on two TECs for cooling it down to $-20°C$ if the ambient temperature is at $22°C$.

Chapter 3

"Beam splitter source" for entangled photons

Within this chapter I will explain the entangled photon source, how to create entanglement, the detection modules and the data acquisition.
The source I developed is a "collinear ppKTP type-II beam splitter source". *Collinear* refers to how the signal and idler beams are leaving the crystal. *PpKTP* denotes the material of the down conversion crystal(KTP = Potassium Titanyl Phosphate) with the periodic poling(pp). *Type-II* refers to the orthogonal polarization of the produced photon pair. In order to get polarization entanglement, the photon pairs are split up on a 50:50 beam splitter and all possible information to distinguish between the signal and idler photons (except their polarization) has to be erased. Three different factors lead to distinguish-ability and need to be considered:

• The pump laser needs a coherence length[1] longer than the length of the down conversion crystal, such that the photon pairs can be created coherently anywhere in the crystal. This was done by choosing the right laser.

• The second requirement is that the photons are degenerate, such that they are not discriminable in wavelength. This can easily be achieved by controlling the temperature of the crystal (described in Chp. 3.2.2).

• The crystal itself is birefringent, therefore the group velocity among the photons of a pair is different. This results in a longitudinal walk-off depending on the position of creation, leading to temporal distinguish-ability. This can be compensated as described in chapter 3.2.3.

[1]The coherence length is the propagation distance over which a coherent wave maintains a specific phase relation, and therefore a stable spatial and temporal interference pattern.

The main reason for choosing this source was the simple setup. Only a few components are required, compared to the more complex sagnac-type[18] and BBO-sources[19]. Therefore it can be built up compact, furthermore the source is mobile and suitable for transport.

3.1 Overview of the experimental setup

The experimental setup of the beam splitter source is shown in Fig. 3.1.

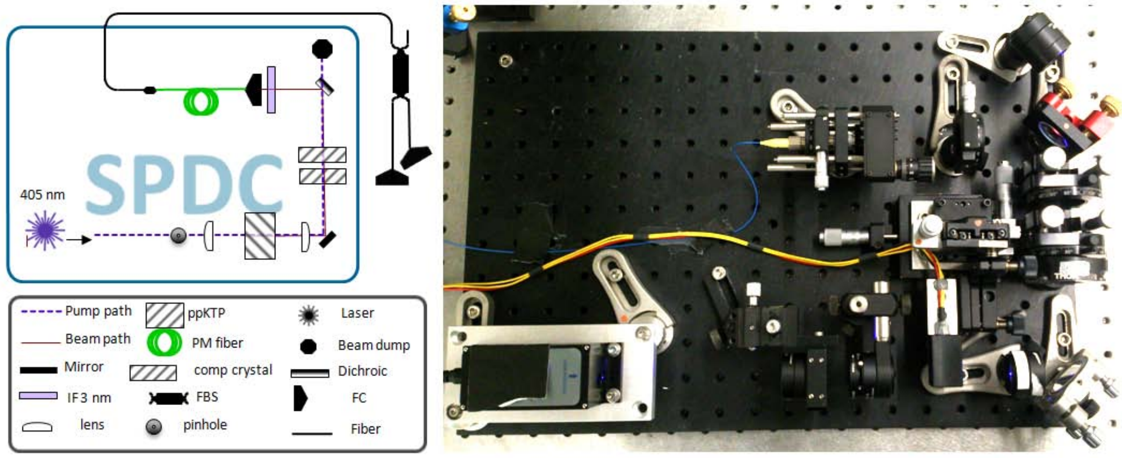

FIGURE 3.1: The scheme on the left and the image on the right show the source with all components(laser, pinhole, focusing lens, covered crystal, collimating lens, compensator crystals, dichroic mirror, HWP, fibre coupler and the PM-fibre(blue)).

The pump laser produced light at a wavelength of 405nm and was focused with a $50mm$ lens into the temperature controlled non-linear ppKTP crystal($10mm$ length) to a spot-diameter of $50\mu m$. Within the crystal, orthogonal polarized photon pairs were produced through SPDC. The photon pairs were collimated with a $50mm$ lens. Three compensator crystals made of Yttrium orthovanadate YVO_4 were placed into the beam path which compensated together with a polarization maintaining(PM) single mode fibre the longitudinal walk off. The dichroic mirror separated the pump beam from the down conversion photons. A $3nm$ interference filter and a colour glass filter blocked remaining unwanted pump light, before the photon pairs were coupled into the PM-fibre. A $50:50$ in fibre beam splitter was attached to the PM-fibre, splitting up a pair with 50% probability. Each output of the BS was connected to polarization analysers.

3.2 Photon generation and walk-off compensation

Subsequently I will explain more in detail the laser, the down conversion crystal and the walk-off compensation.

3.2.1 Laser

In the experiment a Laser from Ondax (LM-405-40) with a nominal power of $40mW$ was used. The data sheet is attached in the appendix C.2. The laser is wavelength stabilized with a volumetric holographic grating (VHG). The centre wavelength of the diode was $405nm$ and the maximum line width of the laser was $0.0875pm(160MHz)$. This results in a coherence length of $60cm$ which is sufficient to produce coherent photon pairs within the $10mm$ long crystal. The beam of the laser had an elliptical shape. In order to achieve a more Gaussian beam profile a pinhole filtered the spatial mode(shown in figure 3.2 and 3.3), resulting in increased coupling to the PM-fibre.

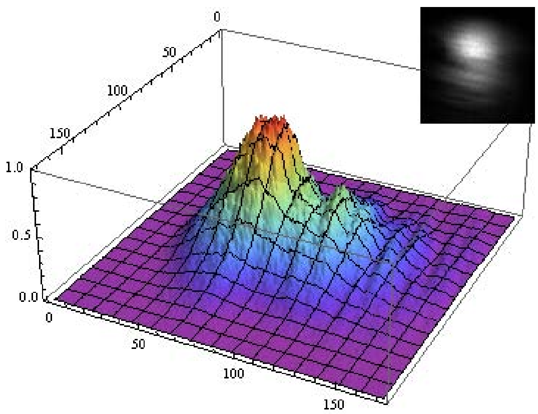

Figure 3.2: The picture of the measured beam profile of the laser(FWHM 350x282μm).

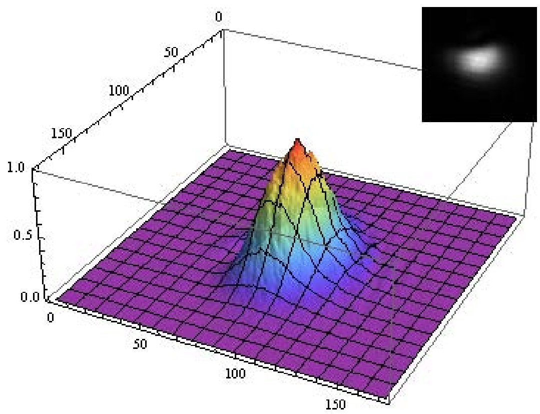

Figure 3.3: The picture of the measured beam profile of the laser cleared with a pinhole(FWHM 244x170μm).

3.2.2 Non-linear crystal

The non-linear crystal for spontaneous parametric down conversion was a $1mm \times 2mm \times 10mm$ periodically poled Potassium Titanyl Phosphate(ppKTP) from Raicol Crystals. The quasi phase matching was achieved due to the periodic poling structure. The poling period Λ was $10.2\mu m$. In order to utilize the highest non-linear coefficient χ_{333} the crystal was pumped parallel to the x-axis with a polarization along in the z-direction.

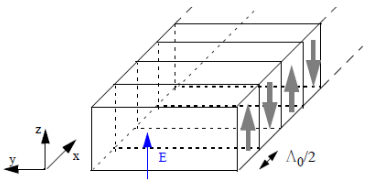

FIGURE 3.4: Scheme of the crystal with the periodic poling responsible for the quasi phase matching. The pump beam should be parallel to the x-axis and polarized along the z-direction(Figure taken from[20]).

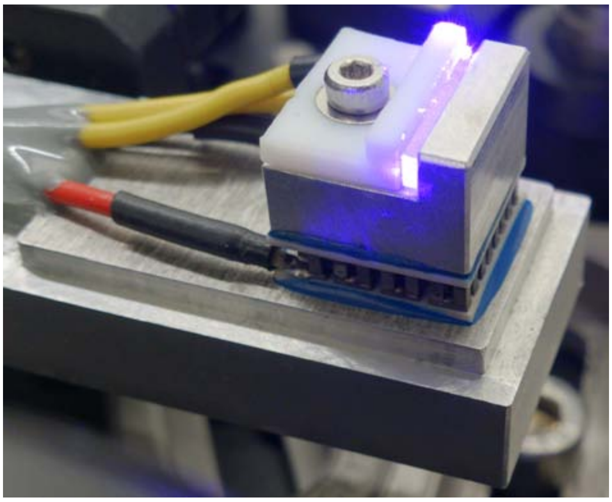

FIGURE 3.5: The picture of the crystal being pumped with a horizontal polarized laser at 405nm. It is mounted on top of a thermo electric coupler and a heat sink.

Temperature control

The temperature of the crystal is very crucial since the wavelength of the SPDC photons changes with $\sim 0.2nm/°C$. In order to set the wavelength of the signal and idler beam to the degenerate case of $810nm$ the crystal had to be temperature controlled. This was achieved by mounting the crystal on top of a thermoelectric heat pump(Peltier element) in addition with a temperature sensor and a PID-controller. Figure 3.6 shows the measured distribution of the signal and idler centre wavelength for different temperatures. It is important for a high visibility [2] that signal and idler match perfectly. Otherwise they would be distinguishable in colour and due to that not entangled. The actual bandwidth $\Delta\lambda_{s,iFWHM}$ of the SPDC photons is given by

$$\Delta\lambda_{s,iFWHM} = \frac{5,52 \cdot 10^{-3}}{L} \cdot nm \tag{3.1}$$

where L denotes the length of the crystal. The bandwidth for a $10mm$ crystal then should be $0.552nm$(FWHM)[21]. The spectra shown in Fig. 3.6 were taken with the single photon spectrometer QE65000 from Ocean Opitcs, which had a limited resolution of $0.4nm$.

[2]The visibilty quantifies the quality of entanglement and is discussed in detail in chapter 4.

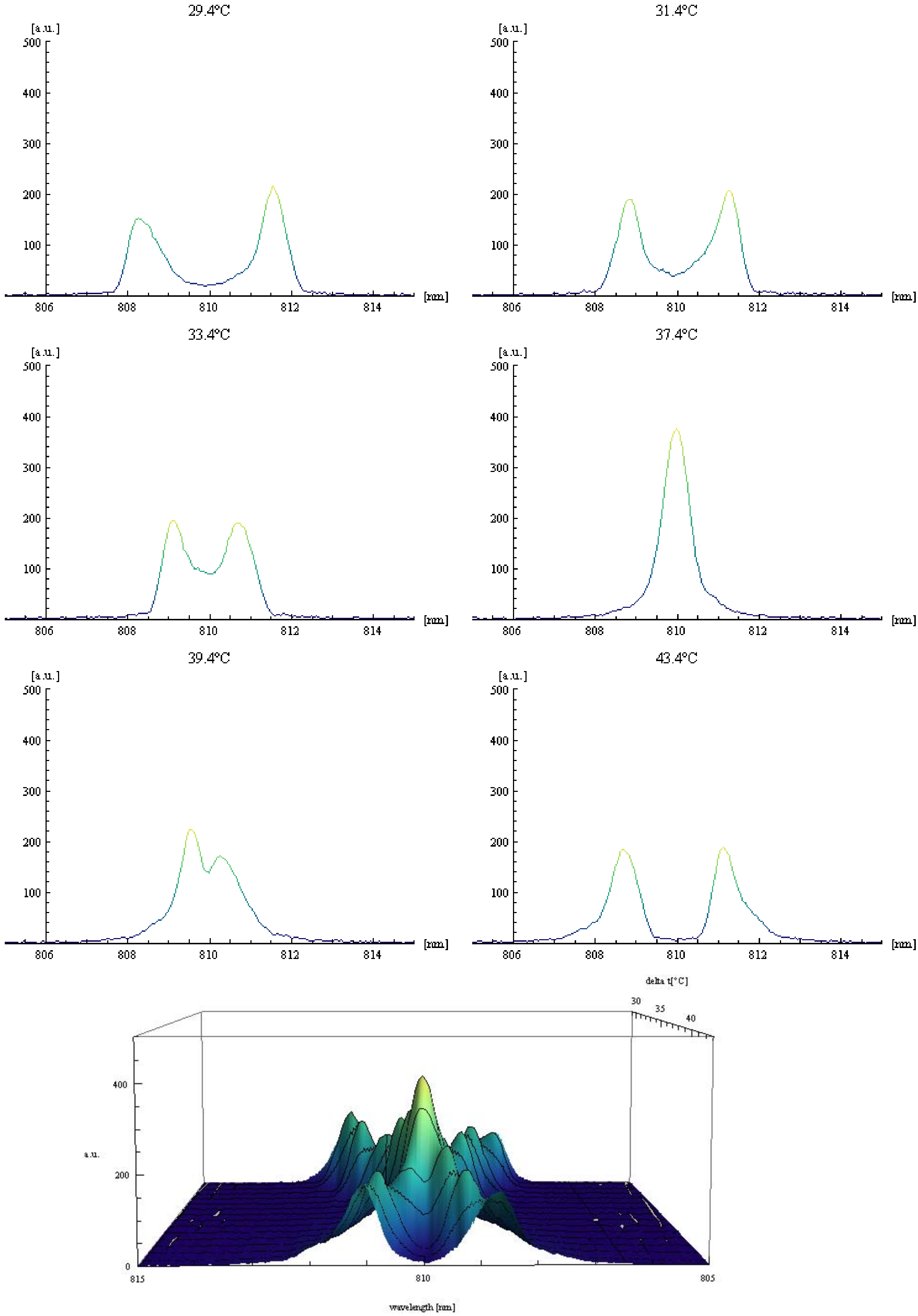

FIGURE 3.6: Wavelength of signal and idler for different temperatures starting from $29.4°C$ to $43.4°C$. On the bottom a 3D-plot illustrates all measured wavelength distributions in one graph.

Additionally, I simulated the temperature distribution within the crystal in an finite element method including convective cooling to see if the temperature is uniformly distributed. I solved the differential equations for the stationary and for the time dependent problem. It seems that the temperature in the crystal is stable after about a minute. This fits very well to the observed behaviour. In figure 3.7 the heat flux and iso-temperature-surfaces are shown. The important thing is that according to this simulation the temperature difference along the axis of propagation is less than $0.1°C$ resulting in negligible wavelength differences of the photon pairs produced at different locations inside the crystal. Hence temperature distribution has no measurable influence on the entanglement quality.

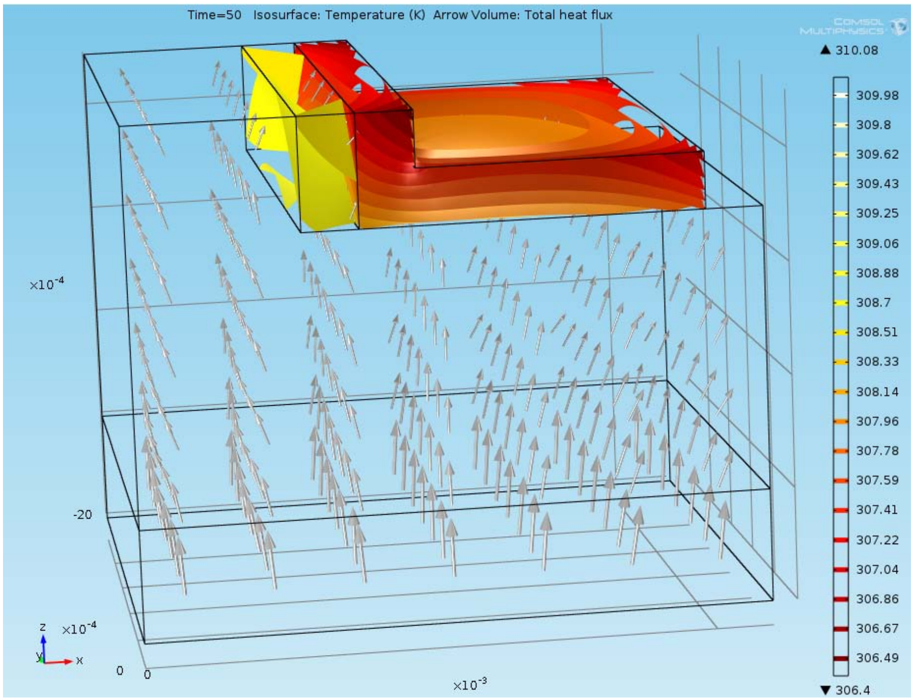

FIGURE 3.7: Image of the calculated heat flux from the oven(at the bottom) to the crystal. The yellowish part is the crystal and the reddish part is a plastic lid for keeping the crystal in place.

3.2.3 Walk-off compensation

The birefringence of the non-linear crystal leads to different propagation speeds of the orthogonal polarized photons and therefore to a longitudinal walk off. Depending on the production position within the crystal the temporal spread between the photons of a pair is different(shown in Fig. 3.8) i.e. a pair generated at the beginning of the crystal gets a maximal walk off compared to no walk off when it is produced at the end. This leads to temporal distinguish-ability depending on the generation location inside the crystal. To erase the information of the production position half of the maximal walk-off needs to be compensated. This then guarantees that for every possible position there exists another production position within the crystal which leads exactly to the opposite walk-off between signal and idler. Hence, one can not know the polarization from the timing difference between the photons.

There are several ways to compensate this walk off. The easiest way is to use the retardation plates of appropriate thickness and orientation, which introduce the desired walk-off between signal and idler photons.

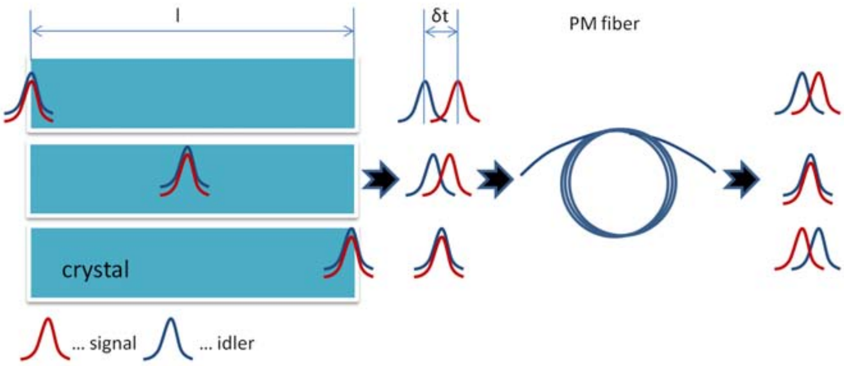

FIGURE 3.8: The longitudinal walk-off due to the birefringence of the crystal and the production position is shown on the left. This was compensated via a birefringent PM-fibre with proper length in addition with retardation plates.

Subsequently the calculation for several birefringent materials is shown, which are suitable to be used as retardation plates. It is not sufficient to consider only the nominal birefringence. One needs to calculate the group velocity v_g because it is often thought of as the speed at which energy or information is conveyed along the wave. The group velocities for the signal and idler beams are given with

$$v_g = \frac{c}{n - \lambda_0 \frac{\partial n}{\partial \lambda_0}}. \tag{3.2}$$

Where n denotes the refractive index of the corresponding material and λ_0 the wavelength in vacuum. The group velocity v_g is calculated using the Sellmaier equations, which show an empirical relationship between the refractive index and the wavelength. The Sellmaier equation for ppKTP is shown in Eq. 3.3 and plotted in Fig. 3.9. All other Sellmaier equations are attached in the appendix B.

$$\begin{aligned} n_y &= \sqrt{2.19229 + \frac{0.83547}{1 - 0.04970\lambda^2} - 0.01621 \cdot \lambda^2} \\ n_z &= \sqrt{2.25411 + \frac{1.06543}{1 - 0.05486\lambda^2} - 0.02140 \cdot \lambda^2} \end{aligned} \tag{3.3}$$

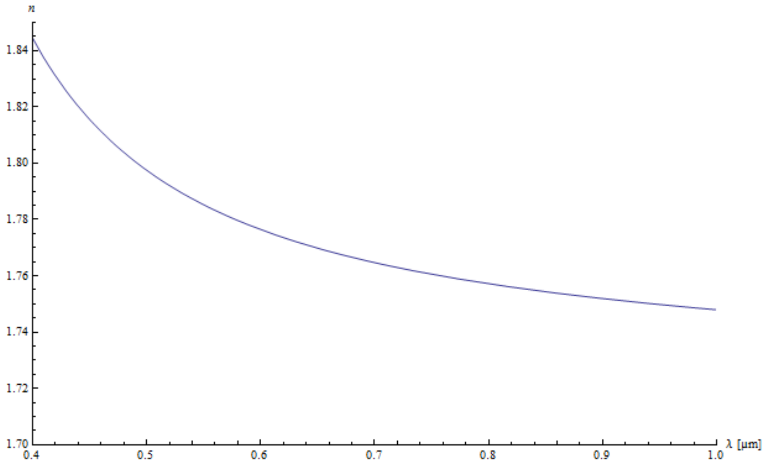

FIGURE 3.9: The calculated graph of the refractive index n_y for ppKTP over the wavelength.

The maximal time difference τ_{max} between the signal and idler photons leaving the crystal occurs when they are generated at the beginning of the crystal:

$$\tau_{max} = (\frac{1}{v_s} - \frac{1}{v_i}) \cdot l \tag{3.4}$$

where l is the length of the crystal. A ppKTP crystal with a length of $10mm$ led to a longitudinal walk off of $3.5 \cdot 10^{-12}s$. The table below shows the length for various other birefringent materials to induce $\frac{\tau_{max}}{2}$. Where n_{gs}, n_{gi} are the refractive indices for the group velocity, Δn is the relative birefringence and Δl is the correct length for compensating the longitudinal walk off for a $10mm$ ppKTP crystal.

	n_s	n_i	n_{gs}	n_{gi}	Δn_g	Δl
ppKTP	1.4806	1.5014	1.8053	1.9105	0.1052	5 mm
Calcite	1.6484	1.4820	1.6732	1.4923	-0.1809	2.908 mm
PM-fibre	1.4531	1.4535	1.4672	1.4668	-0.0004	1.502 m
YVO4	1.9712	2.1847	2.0375	2.2782	0.2407	2.1851 mm
Quartz	1.5328	1.5416	1.5379	1.5470	0.0091	57.523 mm
BBO	1.6603	1.5442	1.6128	1.6839	0.0711	7.4 mm
Magnesium fluoride	1.3750	1.3867	1.4412	1.4802	0.0545	13.498 mm

TABLE 3.1: Table of the calculated refractive index n_s and n_i, group index n_{gs} and n_{gi}, difference of the group index Δn_g and the proper length Δl for compensating the longitudinal walk-off due to a $10mm$ ppKTP crystal for various materials. All indices were calculated for a wavelength of $810nm$.

My approach for compensation at the beginning was a $3mm$ calcite crystal available in the lab, and later on a $1.5m$ PM-fibre with thin YVO4 retardation plates for fine compensation.

Calcite crystal

We used initially an existing calcite crystal for compensation, to check if the source works in principle, even though it had not the correct length, entanglement could be proven for the first time. A visibility of 76.3% in the $|D\rangle/|A\rangle$ measurement basis was achieved. The reason for the low visibility was that the crystal was 23% longer than proper calculated compensation length.

Polarization maintaining fibre

As shown in the table above, there are several different birefringent materials available for compensating the walk off. The reason for choosing the PM-fibre was the advantage, as the name implies that the polarization is maintained and no polarization control is needed. This simplifies further experiments. The PM-fibre is birefringent because of an intrinsic stress induced by stress elements(shown in Fig. 3.10). This elements have a different thermal expansion coefficient than the surrounding glass. This applies after cool down from the production process stress on the fibre along one axis. Due to this the k-vector of the horizontal and vertical polarized photons is slightly different and cross talk between those orthogonal polarizations very low (less than $-40dB$ at $4m$ for an equivalent fibre).
The rotation angle of the fibre at the coupler is very crucial. Already small deviation in the angle led to crosstalk. When the polarized photons are not aligned with the slow and fast axis of the PM-fibre the input polarization is not maintained and therefore contribute to the noise.

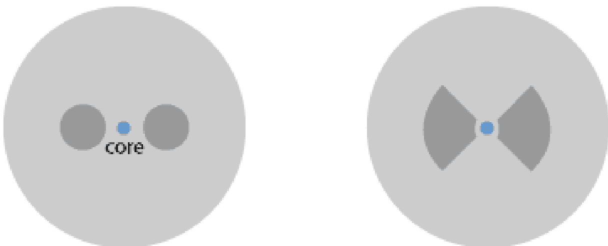

FIGURE 3.10: Polarization-maintaining PANDA fibre (left) and bow-tie fibre (right). The built-in stress elements, made from a different type of glass, are indicated with a darker grey tone(Figure taken from [22]).

Attached in the appendix is the data sheet of the PM630-HP fibre C.1. The relative birefringence of the fibre is $\sim 3.5 \cdot 10^{-4}$. Due to that imprecise value and manufacturing tolerances of the fibre, retardation plates for fine compensation were used. The visibility without the retardation plates in the $|D\rangle/|A\rangle$ measurement basis was 85%.

Retardation plates for fine compensation

The PM-fibre had not the proper length, therefore retardation plates for fine compensation where used in addition. Three retardation plates made out of Yttrium orthovanadate(YVO4) with different thicknesses were ordered. In the end all three together with the PM-fibre were used to compensate the walk-off. The reason for choosing YVO4 was the large birefringence. Therefore the crystals are thin and lead to the smallest beam displacement between the orthogonal polarizations when placed not precisely orthogonal to the beam direction into the beam path. The thickness of all three plates is roughly $\sim 350\mu m$. This value is also due to the production tolerance of $\pm 30\mu m$ for each plate. The visibility with the plates in addition to the PM-fibre was up to 97.5% in the $|D\rangle/|A\rangle$ measurement basis. The rotation angle of the plates is very crucial. When the retarders are not aligned parallel or perpendicular to the polarization of the photons they act like wave plates and the light changes the polarization and the visibility decreases (shown in the Appendix A.1).

3.3 Beam splitter

In the previous chapter I explained how to produce the photon pairs and how to make the photons indistinguishable. In this chapter I will explain how to actually generate the entanglement. Therefore, the crucial element is the beam splitter. If we consider a 50 : 50 beam splitter and a photon is impinging via path a we can quantum mechanically write this as

$$|1\rangle_a \rightarrow \frac{1}{\sqrt{2}}(|1\rangle_c + i\,|1\rangle_d). \tag{3.5}$$

For simplicity, the BS is completely symmetric. The "i" expresses a phase shift of $\frac{\pi}{2}$ between reflected and transmitted wave.

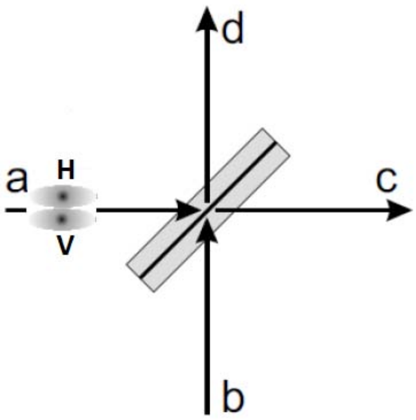

FIGURE 3.11: Two orthogonal polarized photons impinging a 50 : 50 beam splitter via path a (Figure modified from [23]). The generated output state is shown in Eq. 3.6.

If we consider two photons incident on the BS via the same path and in the case of using one horizontal and one vertical polarized, as generated in the ppKTP, the beam splitter operator(Eq. 3.5) transforms this input state $|\phi_{in}\rangle = |H\rangle_a |V\rangle_a$ to

$$\begin{aligned} |\phi_{in}\rangle \xrightarrow{BS} &\frac{1}{2}(|H\rangle_c + i\,|H\rangle_d)(|V\rangle_c + i\,|V\rangle_d) = \\ &\frac{1}{2}(|H\rangle_c |V\rangle_c + i\,|H\rangle_c |V\rangle_d + i\,|V\rangle_c |H\rangle_d - |H\rangle_d |V\rangle_d). \end{aligned} \tag{3.6}$$

Equation 3.6 shows that in 50% of all cases both photons leave the BS in the output c or in d. In the other 50% the photons split up so that they leave the BS in two different outputs. Lets consider only the latter case, the "i" can be neglected as a global phase. Hence, post-selecting on the cases where the photons split up we finally obtain the $|\psi^+\rangle$ Bell State (Eq. 2.7) of the photons in mode c and d. Within the experiments described here, two different BS were used. One was a free-space BS and the other one was an in-fibre beam splitter. The polarization within the fibre is not preserved in general, which made polarization control necessary.

Polarization control

In order to control the polarization in optical fibres, so called "bat ears" can be used. A birefringence is induced by bending the fibre and one can transform any given input polarization state into any desired output state. Within this polarization controller the fiber is coiled up once in the first and in the last paddle and coiled up twice in the middle paddle. Effectively, this can be seen as a quarter/half/quarter wave plate.

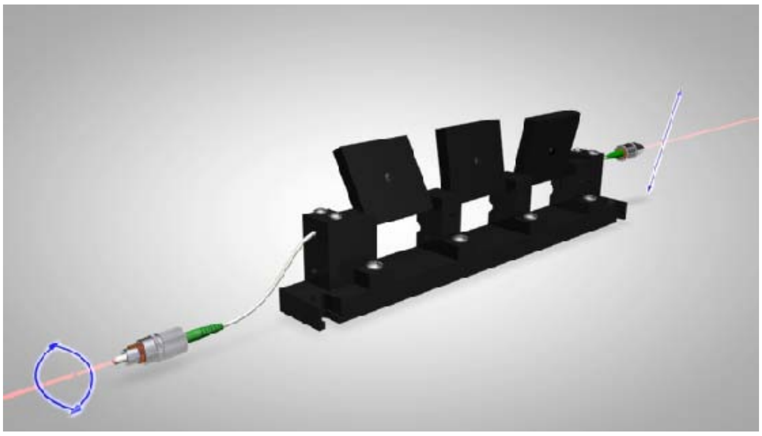

FIGURE 3.12: The image of bat ears for the polarisation control where the incoming polarization is right handed circular and the outcoming polarization is linear(Figure taken from[24]).

3.4 Polarization analysing module

In order to analyse the state and detect the photons, polarization analysing modules were used. Implementing a 50:50 beam splitter allowed as to analyse the photons randomly in one of two measurement basis. Half of the impinging photons on the BS gets reflected and then analysed using a polarizing beam splitter(PBS). Horizontally polarized photons are transmitted at the PBS while vertically polarized are reflected. In this case, the photons are analysed in the $|H\rangle/|V\rangle$ measurement basis. The transmitted photons of the BS are analysed in the complementary polarization basis($|D\rangle/|A\rangle$). This was realized by rotating the polarization of the photons with a half wave plate placed under an angle of 22.5° before the PBS. The photons were detected subsequently on avalanche photo diodes placed in every output of the PBS. The detection signals were recorded with a time tagging module(TTM).

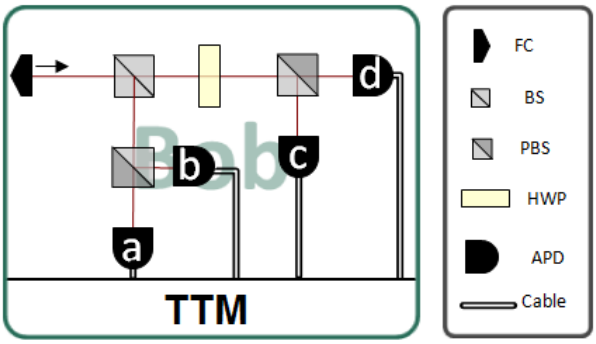

FIGURE 3.13: The scheme of a polarization analysing module, where the photons were analysed in two different measurement basis, and subsequently detected on APDs.

In the experiments described here three different polarization analysing modules were used. The Bob modules I and II were used in the experiment for testing a Bell inequality and the Bob module III was used in the "Bell state test", which will be described later. The schematic for all three Bob modules is the same (shown in Fig. 3.13), the differences are subsequently explained.

3.4.1 Bob module I

The Bob module I was build in an earlier project with colleagues from Munich. It is a free-space module. It is very compact although all optic components, the four detectors and the electronics is build in. In order to use the free-space module in the experiment one output fibre of the beam splitter was attached to a fix focus lens on a XY tip/tilt mount. After aligning it once and shielding it against ambient light, it was also capable to operate at daylight. The BS, PBS and HWP within the module are glued in place, therefore the two detection basis are fixed.

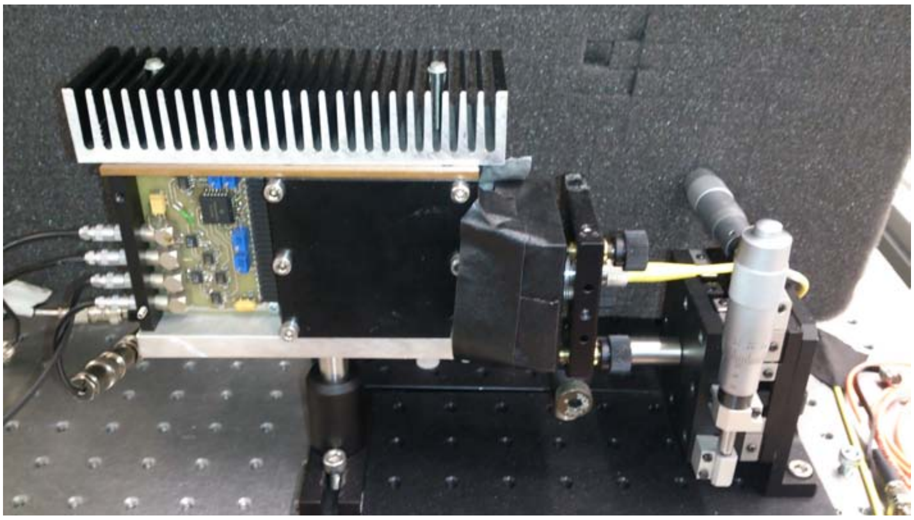

FIGURE 3.14: Image of the free-space bob module I. In order to measure photons from a fibre, a fix focus lens was placed on a a XY tip/tilt mount in front of the entrance filter. The signals of the four diodes are fed into the time tagging module.

3.4.2 Bob module II

This module was developed by my co-worker Matthias Fink. It is explained in detail within his master thesis[25]. The advantage of the very compact design results unfortunately in a hard procedure to align the detectors with the optical components. The second measurement basis $|D\rangle/|A\rangle$ was not adjusted with a half wave plate. It was geometrically tilted by 45 degrees instead. Four small passively quenched single photon detectors from the Austrian Institute of Technology(AIT) were used which were developed within the attempt to build this module.

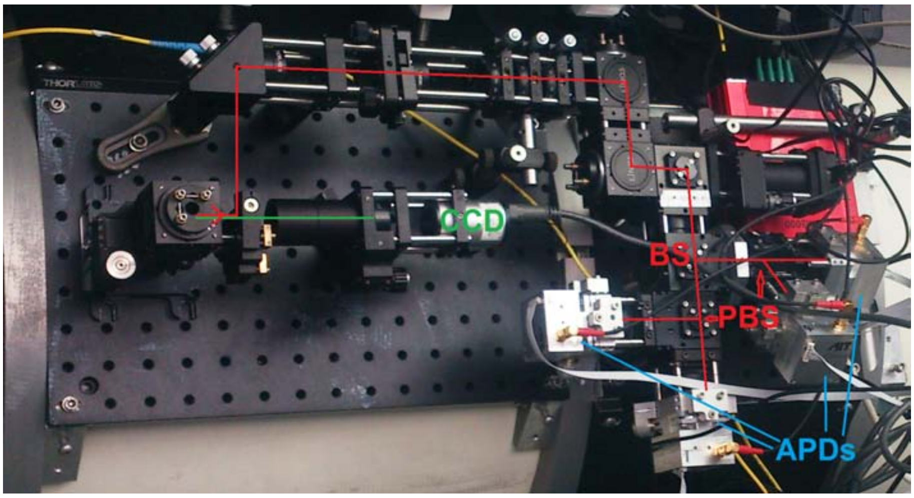

FIGURE 3.15: Image of the Bob module II already attached on the optical ground station in Vienna. The light exits the telescope on the side. At the beginning a dichroic mirror separates the beacon laser ($532nm$) which is sent to a CCD for tracking from the signal light ($810nm$). The signal enters after a mirror and three wave plates for polarization control the bob module. Within the detection module the light is analysed on two PBS in two different measurement basis and detected on APDs from AIT.

3.4.3 Bob module III

This module was used in the "Bell state test". The goal was to realize the in-fibre BS of the source as free-space beam splitter. The PM-fibre was attached directly with a fix focus lens to the module. The fibre beam splitter from the source was replaced through a free-space beam splitter. Every photon was measured in only one measurement basis compared to Bob module I and II where the photons where randomly analysed in two measurement basis as a result of an extra beam splitter. The measurement basis were chosen either with a wave plate in front of the free-space beam splitter for both arms or subsequently the BS for every arm independent. For the second experiment only one motorized HWP was used in front of the beam splitter for rotating both measurement basis from $|H\rangle/|V\rangle$ to $|D\rangle/|A\rangle$. The results are shown in chapter 4.2.

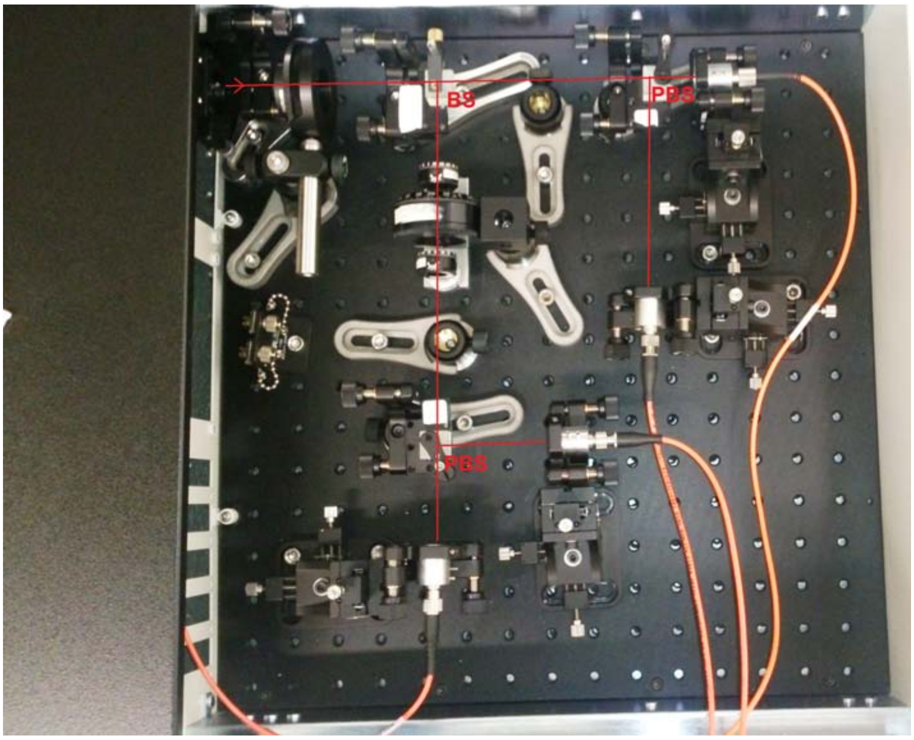

FIGURE 3.16: Image of the Bob Module III. The photons were split up with a BS and guided for polarization analysis in two PBS. The photons were afterwards coupled into multi mode fibres and detected on Perkin Elmer APDs. The module is built within a 19" rack for mobility.

3.5 Data acquisition

In order to find (anti-)correlated photons of the same entangled photon pair, all detected photons on the APDs get an accurate time-stamp by a time tagging module. These time-stamps are further analysed in a personal computer. Detection events within a defined time window(so-called coincidence window) count as coincidences.

3.5.1 Time tagging module

The signals of the avalanche photo diodes where processed in a time tagging module TTM8000 (shown in Fig. 3.17) made by the Austrian Institute of Technology (AIT). This module measures the timing of electronic pulses (rising and/or falling edge) applied on the external digital inputs. The TTM8000 constantly monitors the external inputs and when a transition is detected it records the number of the input, the transition direction and the current value of the high resolution clock in an event table. This table is sent via a Gbit-Ethernet connection to a PC where the events are processed(shown in Fig. 3.18). A screen shot of the Lab View software provided from the Austrian

Institute of Technology is shown in figure 3.20. This software provides a graphical user interface where the count rates are displayed and the user is able to further compute the data(e.g. coincidence evaluation). The time tagging module is usually used in the "I-Mode". This mode supports all eight external inputs with a timing resolution of $82.3045ps(1/12.15GHz)$, an infinite measurement time and is able to count up to $25MEvents/s$[26].

FIGURE 3.17: Image of the front panel of the TTM8000 with the eight input channels and the status LEDs(Figure taken from [26]).

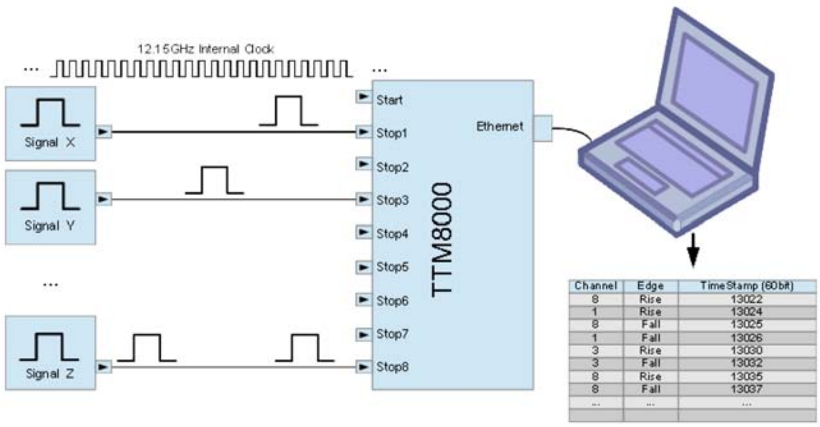

FIGURE 3.18: Scheme of TTM8000. Up tp eight different inputs can be monitored. After a pre set action(rising and/or falling edge)the module sends the channel, the edge and a 60bit time stamp via Ethernet to a computer (Figure taken from [26]).

Timing offset

Different path length in the detection modules, variations in length of fibres and BNC cables lead to timing offsets between the different channels. For a coincidence window in the ns regime this needs to be compensated. A fast way to determine the offsets between two channels is to display a delay histogram (shown in Fig.3.19). This measured offsets are then transferred to the Lab View software for coincidence evaluation (shown in Fig. 3.20).

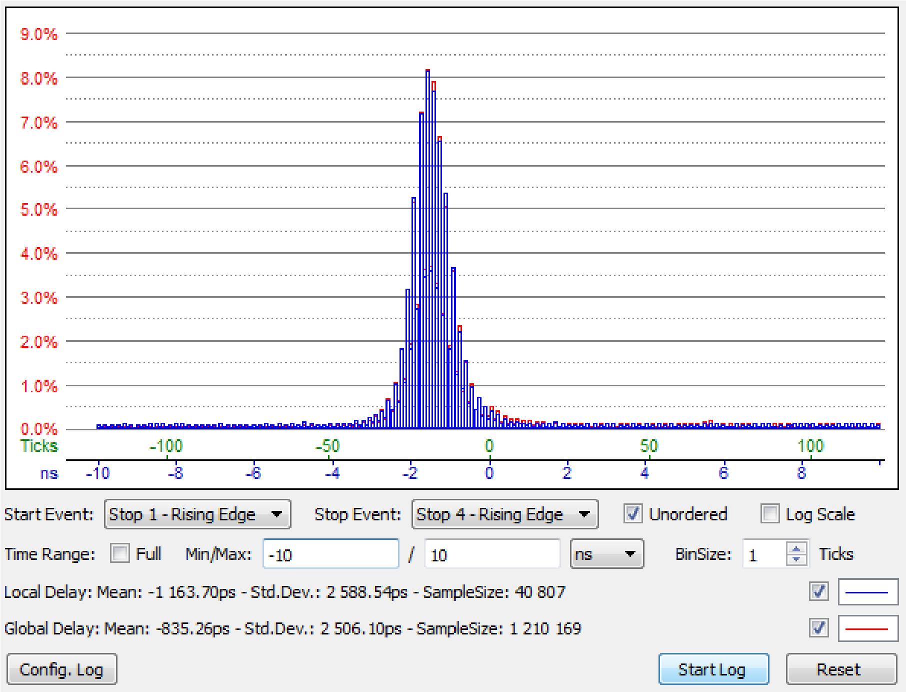

FIGURE 3.19: Image of the delay histogram between channel 1 and channel 4. With this method the delays between the different channels can be measured.

FIGURE 3.20: Screen-shot of the Lab View Software for the TTM8000. On the left side the trigger level can be set separately for each detector. In the second column the proper delay can be set. Coincidences between the individual channels are evaluated according to the logic pattern and the resulting coincidence rates are displayed on the right.

3.5.2 Jitter

Converting an incoming photon into a digital time stamp takes a certain time for the electronics. This "converting time" has an undesired time deviation for each photon, the so called jitter. The smaller the jitter, the shorter the coincidence window can be. This reduces the probability of counting so called accidental coincidences. There is a special mode in the TTM8000 for specific jitter measurements(shown in Fig. 3.21). The time resolution can be set from $1.0ps$ to $27.4ps$ with $10ps$ variance. This is compared to the APDs negligible. The SPDC photons are suitable for measuring the jitter of the detectors, due to their strong temporal correlation down to a few hundred femtoseconds. Let us assume that the jitter has a Gaussian profile and two detectors of the same type have the same jitter variance $\sigma_1 = \sigma_2$. Then one can calculate out of the measured jitter of both detectors σ_s the jitter for one detector as follows

$$\sigma_1 = \frac{\sigma_s}{\sqrt{2}}. \tag{3.7}$$

This formula is derived in the appendix A.3. In the following table the measured variance σ_s and the calculated jitter for three different avalanche photo diodes is shown.

	σ_s	σ_1
AIT APD	1.15ns	0.81ns
BOB I APD	1.28ns	0.91ns
Perkin Elmer APD	0.47ns	0.33ns

TABLE 3.2: Table of the measured jitter σ_s between two identical detectors and the back calculated jitter for one detector σ_1 according to Eq. 3.7.

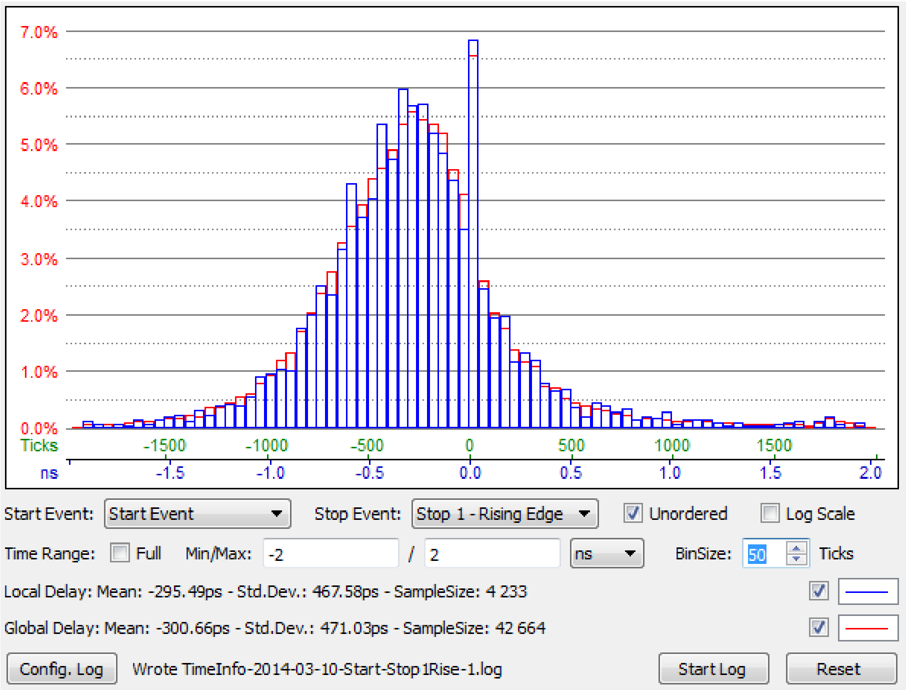

FIGURE 3.21: Image of a start-stop measurement between two Perkin Elmer diodes. The software from the TTM8000 fits automatically a Gaussian and displays the standard deviation σ_s of the summed up jitter.

Chapter 4

Results

Within this chapter the results of two different experiments are shown. The first experiment was a fundamental test about violating the Bell inequality, and therefore a proof of entanglement. The second experiment was about measuring the "intrinsic" Bell state generated by the source, which is important for further experiments.

4.1 Violation of the Bell inequality

For this experiment the entangled photons from the source where guided with SM-fibres to two polarization analysing modules(Bob module I and II). The setup for the experiment is shown in Fig. 4.1.

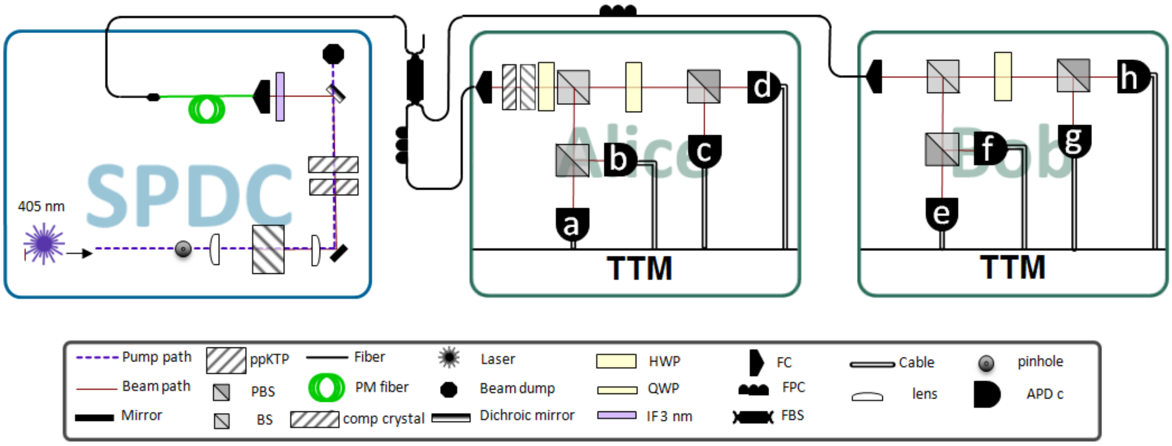

FIGURE 4.1: Schematic view of the entangled photon source connected to the two polarization analysing modules. A half wave plate rotated the measurement basis of one analysing module to the proper "bell test angles". The phase for the Bell state was controlled by tilting one of two crossed crystals in front of one Bob module.

For a maximal violation of the CHSH form of the Bell inequality the "Bell test angles" mentioned in chapter 2.4 were used. Therefore in front of one bob module a half wave plate rotated both measurement basis by 22.5°. It order to set the desired Bell state, the phase ϕ in equation 4.1 needs to be controlled. This was done by tilting one of two equally long crossed compensator crystals[1] which were placed in front of the HWP.

$$|\psi^{\pm}\rangle_{12} = \frac{1}{\sqrt{2}}) |H\rangle_1 |V\rangle_2 + e^{i\phi} |V\rangle_1 |H\rangle_2) \tag{4.1}$$

4.1.1 S-value

Detecting the entangled photons in two different mutual unbiased basis in each arm allowed us to measure the S-value in real time. After a $865min$ long-run measurement the S-value was 2.512 ± 0.000284 which was 1805 standard deviations away from the classical S-value of 2. For illustration, it is more likely to win 100 000 times the Austrian lottery in a row than this result is accidentally true.

$$\sigma_{violation} = \frac{S^{exp} - 2}{\sigma} = \frac{2.512 - 2}{0.000284} = 1805 \tag{4.2}$$

Table 4.1 lists the measured and predicted P and S values with the corresponding angles.

results		
	measured values	predicted values
$P(0°, 22.5°) =$	-0.592	-0.71
$P(0°, 67.5°) =$	-0.628	-0.71
$P(45°, 22.5°) =$	0.689	0.71
$P(45°, 67.5°) =$	-0.603	-0.71
S=	**2.512**	**2.83**

TABLE 4.1: The table lists the measured and predicted P and S values.

The graphs in figure 4.2 and 4.3 show the time evolution of $\sigma_{violation}$ and the P values, respectively.

[1]The crystals were crossed to ensure that the have no influence on the walk-off compensation itself and alter only the phase.

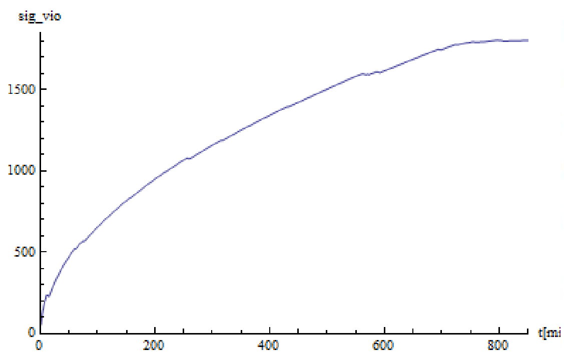

FIGURE 4.2: Graph of the measured number of sigma violation over time.

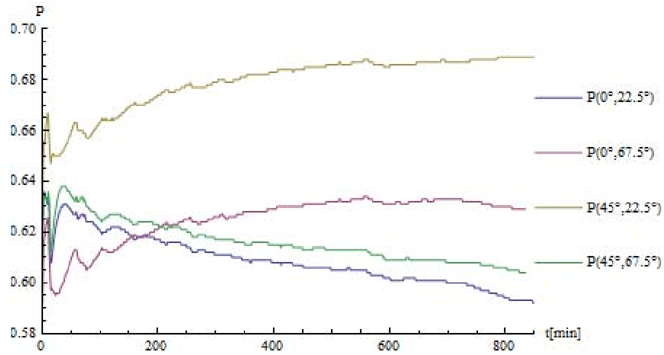

FIGURE 4.3: Graph of the modulus of the four measured P values over time.

4.1.2 Singles and visibility

Within this experiment neutral density(ND) filters reduced the laser power in order not to saturate the passively quenched detectors(which were used in Bob module I and II) and to achieve a good visibility. The count rates from the experiment are shown in figure 4.4. The fluctuations on all count rates are the very same, so this should be a result of temperature changes in the room and therefore changing the coupling from the 810nm photons into the fibre. In order to quantify the setup, the visibility V can be calculated out of the measured S-value S^{exp} as follows

$$V = \frac{S^{exp}}{S^{qt}_{max}}. \tag{4.3}$$

The averaged visibility over the whole measurement run was 88.7%. The graph in Fig. 4.5 shows the time averaged visibility(blue). One can see that in the end after almost 14 hour long measurement the actual visibility(magenta) significantly dropped. This is a result of polarization drift in the fibres. This also increases the error and therefore the stagnation in the $\sigma_{violation}$ at the end of the measurement run(shown in Fig. 4.2).

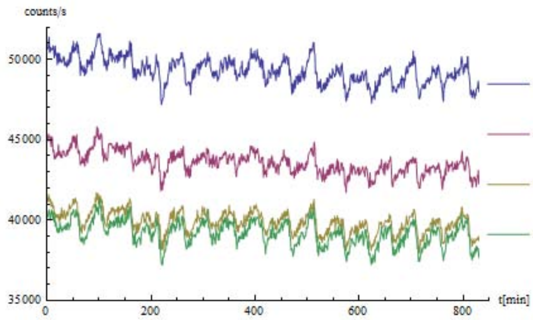

FIGURE 4.4: Graph of the measured count rates of $|H\rangle$ and $|D\rangle$ polarisation of both detection modules over the 865min measurement run.

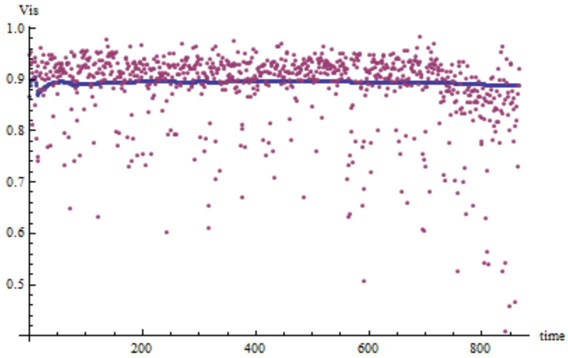

FIGURE 4.5: Graph of the measured averaged visibility(blue) and the actual visibility(magenta) over the time.

It is also possible to calculate the visibility out of the coincidences as follows

$$V = \frac{C_{max} - C_{min}}{C_{max} + C_{min}}. \tag{4.4}$$

Where C_{max} and C_{min} denotes the coincidences in the maximum and minimum respectively. In case of an anti-correlated Bell state ($|\psi^-\rangle_{12}$) the C_{max} is the sum of C_{DA} and C_{AD}, whereas C_{min} is the sum of C_{DD} and C_{AA}, respectively. The two indices refer to the measured polarization state of the two photons. Therefore the visibility is given with

$$V = \frac{(C_{DA} + C_{AD}) - (C_{DD} + C_{AA})}{(C_{DA} + C_{AD}) + (C_{DD} + C_{AA})}. \tag{4.5}$$

In a perfect setup a maximal entangled state leads to zero coincidences in the minimum. In the real experiment imperfections in the crystals, fibres, beam splitters, polarizing beam splitters and walk off compensation contribute to this coincidences C_{min}, just as the accidental coincidences. They occur when a coincidence is detected between two photons which do not come from the same pair. This can be a single-single, single-dark or dark-dark count event. The dark count rates of the detectors are negligible, therefore the largest part in my experiment reducing the visibility were the accidentals A, when two photons from different pairs hit the detectors within the coincidence window. They are calculated as follows

$$A = S_1 \cdot S_2 \cdot \tau \tag{4.6}$$

where S_1 and S_2 are the single count rates of the detectors in the two arms, and τ is the coincidence window. Assuming a perfect setup and a maximally entangled state only half of the accidentals contributed to C_{min} whereas the other half of the accidentals contributes to the C_{max}. C_{max} can be expressed as Singles S_1[2] from one detector times the coupling ν ($\nu = \frac{(C_{max}+C_{min})}{S_1} \sim \frac{C_{max}}{S_1}$). This leads to the following equation

$$V = \frac{\left(S_1 \cdot \nu + \frac{S_1 \cdot S_2 \cdot \tau}{2}\right) - \frac{S_1 \cdot S_2 \cdot \tau}{2}}{\left(S_1 \cdot \nu + \frac{S_1 \cdot S_2 \cdot \tau}{2}\right) + \frac{S_1 \cdot S_2 \cdot \tau}{2}} = \frac{S_1 \cdot \nu}{S_1 \cdot \nu + S_1 \cdot S_2 \cdot \tau} = \frac{1}{1 + \frac{S_2 \cdot \tau}{\nu}}. \tag{4.7}$$

The equation above was plotted in a 3D graph for a coincidence window of $1ns$.

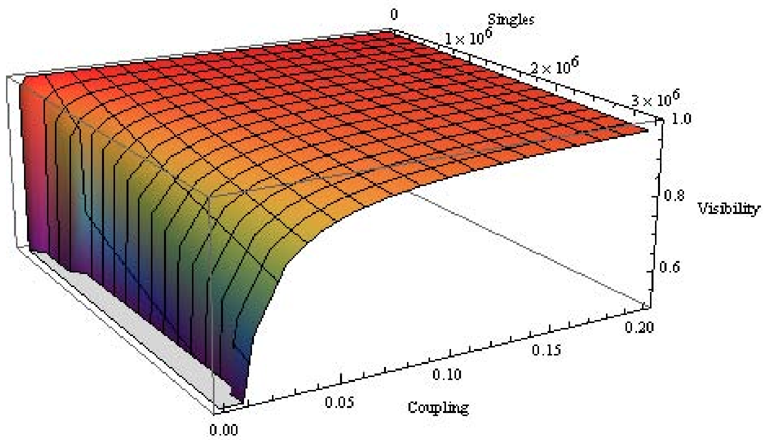

FIGURE 4.6: Graph of the calculated visibility maximum achievable considering accidentals with a coincidence window of 1ns.

The graph and the equation 4.7 clearly show, in order to get a good visibility one need to reduce the singles and the coincidence window τ and improve the coupling.

[2]This only applies when the two countrates $S_1$and S_2 are balanced.

4.2 Bell state test

In this so called "beam splitter source" altering the phase ϕ of the Bell state is only possible after the photons are split by the beam splitter. For this experiment, all the birefringent elements, which could influence the relative phase between signal and idler photons, after the beam splitter have been removed to observe the "intrinsic" Bell state of the source. Hence, the polarization maintaining fibre was plugged directly into module III (shown in Fig. 3.16). Since this is a free-space realization, there is no drift of the polarization such as in fibres, therefore no polarization control was needed. At full laser power a maximum of 2.4 million singles/s per channel was achieved. With a coupling of 13% this resulted in 312 000 coincidences/s with a visibility of 88% in the $|D\rangle/|A\rangle$ measurement basis and 95.1% in the $|H\rangle/\ |V\rangle$ measurement basis, respectively. With a HWP in a motorized stage in front of the beam splitter both measurement basis were rotated equally. Only one measurement basis was used in every arm after the BS compared to the Bell inequality violation experiment.

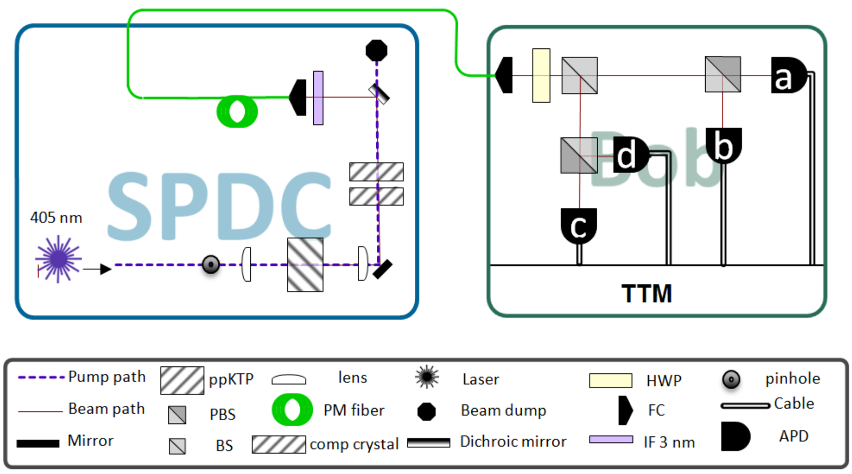

FIGURE 4.7: The source was connected via PM-fibre directly to the free space bob module. A motorized half wave plate was used in front of the beam splitter for rotating the measurement basis.

In the $|H\rangle/|V\rangle$ measurement basis the state showed anti-correlations whereas in the $|D\rangle/|A\rangle$ measurement basis correlations(shown in Fig. 4.8).

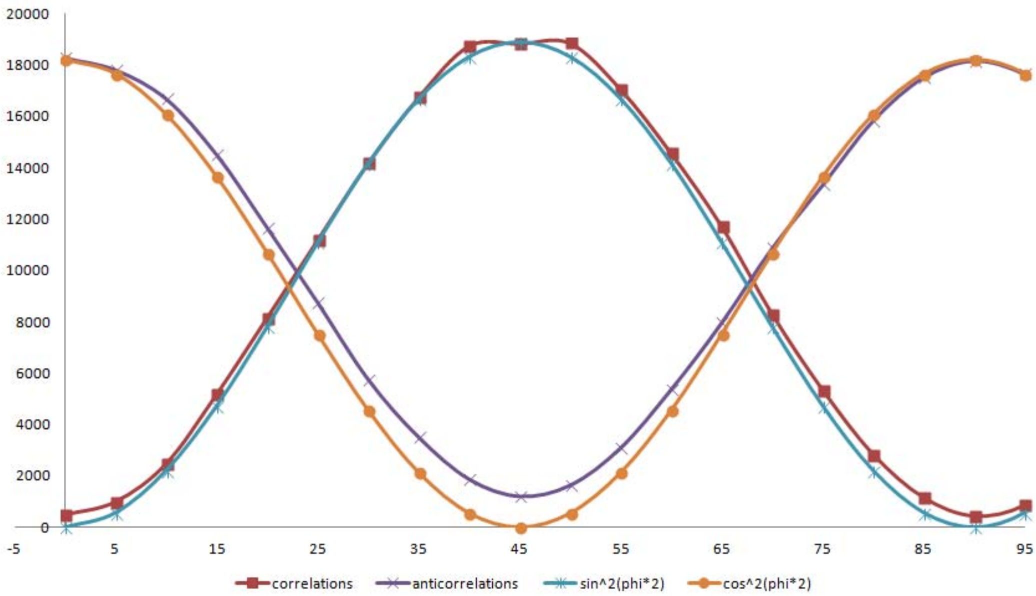

FIGURE 4.8: Graph of count rates of correlations, anti-correlations, a fitted $sin^2\phi$ and $cos^2\phi$ over the rotation angle ϕ of the measurement basis. 0° and 90° indicate the $|H\rangle$ $|V\rangle$ measurement base whereas 45° the $|D\rangle/|A\rangle$ base respectively.

The measured behaviour belongs to a $|\psi^+\rangle$ Bell state as predicted in chapter 3.6.

$$|\psi^+\rangle_{12} = \frac{1}{\sqrt{2}}(|H\rangle_1 |V\rangle_2 + |V\rangle_1 |H\rangle_2) = \frac{1}{\sqrt{2}}(|D\rangle_1 |D\rangle_2 - |A\rangle_1 |A\rangle_2). \tag{4.8}$$

A $|\psi^-\rangle$ Bell state is rotation invariant and would show anti-correlations independent of the measurement basis.

Chapter 5

Quantum Experiments at Space Scale

This chapter describes the Quantum Experiments at Space Scale (QUESS) project, the satellite, the optical ground stations and the tracking. Within this project we want to establish a satellite to ground link for quantum key distribution. This project is a collaboration between the Chinese Academy of Science(CAS) and the Austrian Academy of Science(AAS). The CAS will launch a dedicated satellite in 2016. Based on a cooperation contract, our institute was invited to be part of these experiments providing four optical ground stations within Europe. Those stations are located in Vienna, Graz, Kephalonia and Tenerife.

5.1 Satellite

To our knowledge the satellite launched by the Chinese Academy of Science will have two different photon sources for quantum key distribution on board. One is a decoy source which distributes a key according to the BB84 protocol described in chapter 2.5.1. The second one is an entangled photon source, which utilizes the entanglement based BB84 explained in chapter 2.5.2. The satellite will be in a sun synchronous low earth orbit(LEO) at 600km with an inclination of 97.79° and a mass of $\sim 600kg$. This should lead to period of $90min$ and a link duration of 200 seconds per flyover.

5.2 Optical ground stations

The optical ground stations together with a polarization analysing module should receive the quantum signal from the satellite. Subsequently the four ground stations in Europe are explained.

5.2.1 Vienna

On the top of the Institute for Quantum Optics and Information(IQOQI) in Vienna is placed a $40cm$ Newton telescope with a focal lenght of $120cm$. This serves as testbed for the setups for the final experiments. It is almost fully equipped. This includes a bob module with two measurement basis, time tagging unit and a tracking CCD-camera.The dome and the telescope were lifted up with a crane on the 17th of April in 2013. Since then a lot of equipment was mounted additionally and therefore a lot of extra weight. The stepper motors of the mount are already at the limit, this makes satellite tracking less feasible. Considerations about buying a new telescope have been done.

Figure 5.1: The bare telescope after installation on the equatorial mount.

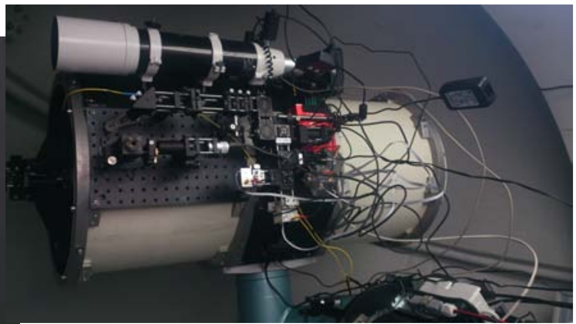

Figure 5.2: OGS Vienna fully equipped with a EOS 500 attached to a finder telescope, the Bob module II and the TTM8000.

Figure 5.3: Picture of the optical ground station Vienna on the rooftop of the IQOQI from the outside.

5.2.2 Graz

The telescope in Graz is altazimuth mounted and has an aperture of $50cm$. It is usually used for laser ranging on satellites and space debris. We already equipped the telescope with a polarization analysing module and conducted first measurements via a corner reflector.

FIGURE 5.4: Picture of the telescope in Graz on an altazimuth mount with the detection package already attached.

5.2.3 Tenerife

The OGS Tenerife(Spain) is located at the Teide observatory at 2400m above sea level and it was built and is still owned by ESA(European Space Agency). The primary mirror has an aperture of $1m$ and it has two different foci. One can either use the Cassegrain focus with a focal length of 13.3m or the Coudé focus with a focal length of 38.95m (shown in Fig. 5.5). The original purpose of the station is to perform in-orbit test of laser telecommunications terminals on board of satellites in low earth - and geostationary orbits. Although it was already used as receiving station in several quantum experiments.

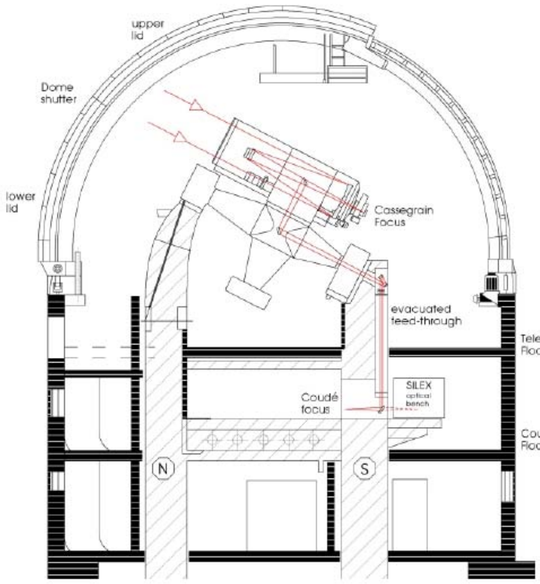

FIGURE 5.5: Scheme of the cross section from the OGS in tenerife with the Cassegrain focus (focal length 13.3m) and the Coudé focus (focal length 38.95m)(Figure taken from [2]).

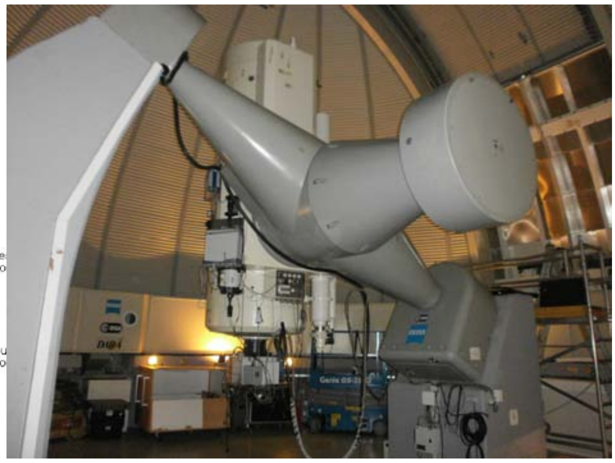

FIGURE 5.6: Image of the telescope with the equatorial mount and a camera attached on the Cassegrain path.

5.2.4 Kephalonia

The altazimuth mounted telescope in Kephalonia (Greece) is the biggest and newest within the QUESS project with a diameter of 1.4m and an effective focal length of 16.8m. The primary mirror deforms due to gravity depending on the position. At the back of the primary mirror are several actively controlled pistons attached to counteract the deformation. It has a Nasmyth and a Cassegrain focus.

FIGURE 5.7: Image of the housing of the newest telescope in the QUESS project. It is located in Kephalonia in Greece at a height of 1060m above seelevel.

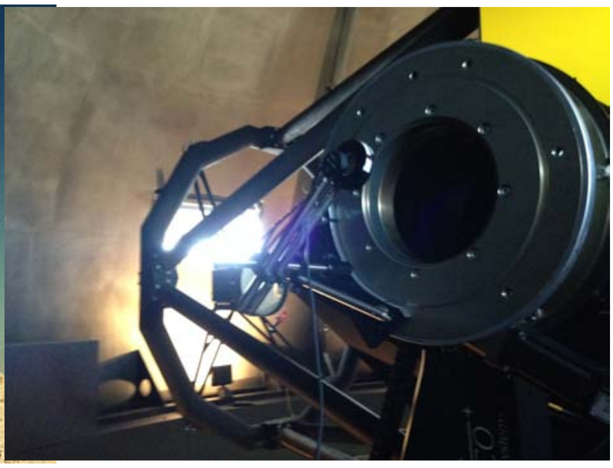

FIGURE 5.8: Image of the secondary mirror of the 1.4m telescope and the Nasmyth focus were already a polariser and a power meter for polarization measurement is attached.

5.3 Tracking

The satellite has an angular velocity(in the reference frame of the OGS) of $0.1°/s$ when it is ascending/descending at the horizon. The angular velocity is maximal at the zenith with $0.7°/s$. This together with the inaccurate known orbit of the satellite makes tracking necessary. Therefore the satellite sends a green beacon laser at a wavelength of $532nm$ in parallel to the quantum signal at $850nm$. This beacon laser is then imaged with a CCD-camera. A feedback control loop keeps this received spot on a predefined reference point on the camera by controlling the motors of the telescope mount. This guarantees that the focused spot of the quantum signal stays on the detectors. The beacon laser of the satellite has only an intensity of $0.1nW/m^2$ in the worst case on ground. The subsequent table shows the collected photons/s of the beacon laser for the different telescope sizes.

	ø primary	ø secondary	eff. area	photons/s
OGS Vienna	0.4m	0.1m	$0.118m^2$	31 500 000
OGS Graz	0.5m	0.15m	$0.179m^2$	47 800 000
OGS Kephalonia	1.4m	0.2m	$1{,}51m^2$	404 000 000
OGS Tenerife	1m	0.2m	$0.754m^2$	200 000 000

TABLE 5.1: The table lists the diameter of the primary and secondary mirror, the calculated effective area and the expected photons per second of the green beacon laser for all four European Optical Ground Stations.

The smallest telescope in Vienna collects in the worst case only 31 million photons per second. Whereof 90% are imaged on the CCD for tracking purpose and the other 10% are detected on an APD and used for timing. Due to that a highly sensitive camera must be used.
To investigate the functionality of different CCD cameras at this low light level, we set up a camera test stand(shown in Fig. 5.9). A green free space laser diode was coupled into a fibre. After the fibre an adjustable attenuator (Aigilent 8166B) was used. To measure the photon flux in real time a in-fibre beam splitter with a ratio of 1 : 10 was used. On one output of the beam splitter the photons were measured with a Perkin Elmer APD. The other output from the BS was attached to a fix focus lens. This beam was focused on different cameras with a $35mm$ plan convex lens. The spot on the camera was varied from $5\mu m$ to $100\mu m$ and the image was simultaneously displayed in addition with the count-rate of the diode.

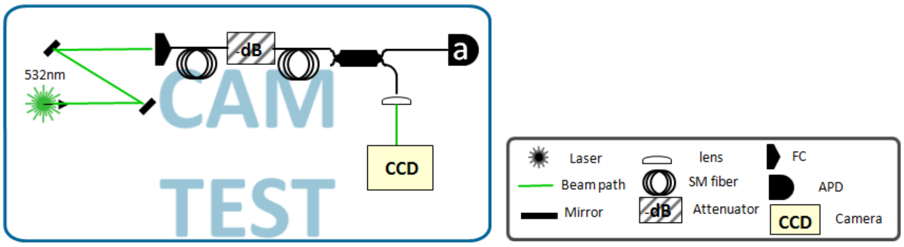

FIGURE 5.9: The scheme depicts the setup of the camera test stand. A green laser is coupled into a fibre, attenuated and split into two paths where one is detected on a APD and the other path is guided on a CCD-camera.

In order to quantify the sensitivity of the camera the peak significance S_p of the observed spot image was calculated as follows

$$S_p = \frac{s_p - s_{avg}}{\sigma} \tag{5.1}$$

where s_p denotes the amplitude of the peak, s_{avg} the averaged background-level and σ the standard deviation of the Gaussian fit. The most promising camera was the VLG-22m from Baumer. It was able to image a spot with $100\mu m$ at a exposure time of $100ms$ and a photon flux of $8 * 10^6$photons/s. The peak significance was 47.3 in the x-direction and 27.7 in the y-direction, respectively. This exposure time leads to a frame rate of $10Hz$. According to our colleagues in Graz, this is sufficient to track a satellite, although higher frame rates make the feedback control loop more precise.

Chapter 6

Conclusion and outlook

The reason for choosing the "beam splitter source" was its simplicity. This results in a very compact setup due to just a few components required. The whole source was already transferred into a 19" rack and therefore it is easily transportable. It seems that the polarization maintaining fibre has not the proper length. This is in my opinion a consequence of the roughly known value of the nominal birefringence of the PM-Fibre. So even with the compensator crystals the maximum visibility was "only" 97%(with accidental subtraction) in the $|D\rangle/|A\rangle$ basis. This is still not bad, but there is still some space left to improve. One disadvantage of the beam splitter source is the maximal theoretical coupling of 50%. This decreases as previously discussed also the visibility.

For more lossier links, it is possible to increase the SPDC rate, by increasing the length of the crystal. A new oven design which is capable to keep crystals up to length of $25mm$ would be useful. A longer crystal would make it easier to compensate the longitudinal walk-off as a result of a smaller bandwidth and therefore a longer coherence time. Whereas the temperature control needs to be more precise then. This needs still to be checked if the current oven controller is able to handle this.

In order to pretest the receiving telescopes and its components the "beam splitter source" together with a transmitter setup should be used. One example for such a transmitter telescope is shown in figure 6.1.

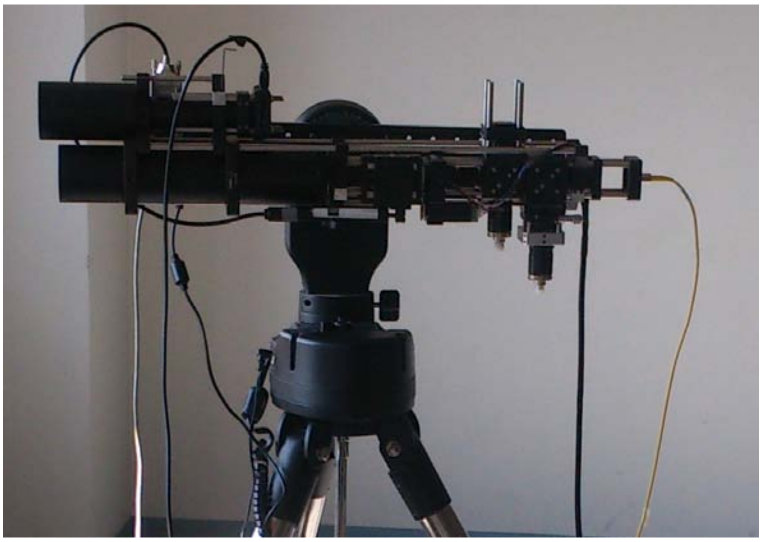

Figure 6.1: Picture of the transmitter setup mounted on a tripod.

The PM-fibre of the BS-source will be attached directly to the sending telescope together with a free space bob module mounted on the setup. This is a powerful tool to test the optical ground stations via a horizontal link. Because this arrangement would be very mobile and robust as a result of the polarization maintaining fibre and the fact that the phase can not be altered before the beam splitter. The testing can be done directly from the OGSs with the help of a corner cube or from a place which is within the range of motion of the telescope(e.g. a small hill because usually the telescopes are not designed to look at the horizon or below). In Vienna and Graz suitable corner cubes are already applied.

We are confident that with the "beam splitter source" we are able to test and prepare the optical ground stations. So that they are operational when the satellite is in orbit and we can distribute a quantum key and furthermore make the whole QUESS project to a successful one.

Appendix A

Miscellaneous

A.1 Wave plates

Wave plates are usually birefringent optical devices which change the polarisation state of the propagating light wave. Two common wave plates are the quarter- and half wave plate. The half wave plate shifts the polarization direction of linear polarized light and the quarter wave plate converts linearly polarized light into elliptically or circularly polarized light. The gathered phase shift Γ depends on the birefringence Δn the thickness of the crystal L and the vacuum wavelength λ_0 of the light.

$$\Gamma = \frac{2\pi \Delta n L}{\lambda_0} \tag{A.1}$$

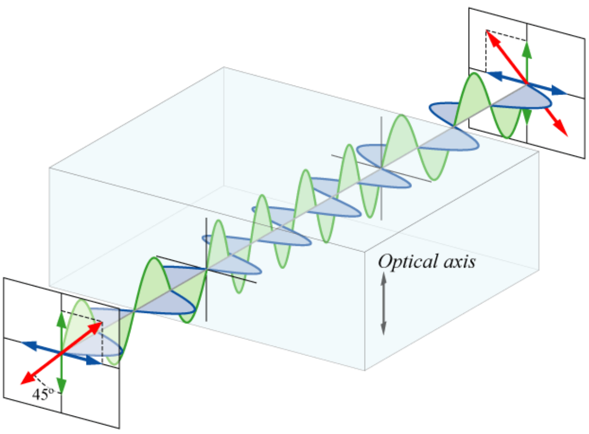

FIGURE A.1: Schematic of a half walf plate. The entering light can be resolved into two waves, parallel(green) and perpendicular(blue) to the optical axis. The green wave propagates slightly slower than the green one. At the end of the plate the relative delay is exactly half of a wavelength resulting in a 90 degree shift of the input polarization state.

Γ is for a half wave plate π, for a quarter wave plate $\frac{\pi}{2}$ and unknown for the retardation plates.

A.2 Error propagation

In order to get the statistical value from the bell value:

$$S := |P(\vec{a}, \vec{b}) - P(\vec{a}, \vec{b'})| + |P(\vec{a}', \vec{b'}) - P(\vec{a}', \vec{b})| \leq 2. \tag{A.2}$$

with P defined as follows

$$P_{(\alpha,\beta)} = \frac{N_k(\alpha,\beta) - N_k(\alpha,\beta^{\perp}) - N_k(\alpha^{\perp},\beta) + N_k(\alpha^{\perp},\beta^{\perp})}{N_k(\alpha,\beta) + N_k(\alpha,\beta^{\perp}) + N_k(\alpha^{\perp},\beta) + N_k(\alpha^{\perp},\beta^{\perp})} \tag{A.3}$$

it is useful to define two new values N_p and N_s

$$\begin{aligned} N_p &= N_p(\alpha,\beta) = N_k(\alpha,\beta) + N_k(\alpha^{\perp},\beta^{\perp}) \\ N_s &= N_s(\alpha,\beta) = N_k(\alpha,\beta^{\perp}) + N_k(\alpha^{\perp},\beta). \end{aligned} \tag{A.4}$$

The error of the single coincidence rates follow a poisson distribution

$$\Delta N_k = \sqrt{N_k} \tag{A.5}$$

The expectation value of P is

$$P = \frac{N_p - N_s}{N_p + N_s} \tag{A.6}$$

and the corresponding error is

$$\Delta P = \sqrt{\left(\frac{\partial P}{\partial N_p}\Delta N_p\right)^2 + \left(\frac{\partial P}{\partial N_s}\Delta N_s\right)^2} = \frac{2\sqrt{N_p^2 N_s + N_p N_s^2}}{(N_p + N_s)^2} \tag{A.7}$$

with $N := N_p + N_s$

$$\Delta P = \sqrt{\frac{1}{N}(1 - P^2)} \tag{A.8}$$

and finally

$$\Delta S = \sqrt{\Delta P(\alpha,\beta)^2 + \Delta P(\alpha,\beta')^2 + \Delta P(\alpha',\beta)^2 + \Delta P(\alpha',\beta')^2}. \tag{A.9}$$

A.3 Convolution

The convolution is a mathematical operator often used in signal analysis (e.g jitter measurement chapter 3.5.2) and image processing. The convolution of two functions f and g is defined as the integral of the product of the functions where one is reversed and shifted

$$(f * g)(t) := \int_{-\infty}^{\infty} f(\tau)g(t-\tau)d\tau. \tag{A.10}$$

The convolution of two Gaussian functions is again a Gaussian function.

$$f(t) = \frac{e^{\frac{-(t-\mu_1)^2}{2\sigma_1^2}}}{\sigma_1\sqrt{2\pi}} \tag{A.11}$$

$$g(t) = \frac{e^{\frac{-(t-\mu_2)^2}{2\sigma_2^2}}}{\sigma_2\sqrt{2\pi}} \tag{A.12}$$

$$f * g = \frac{e^{\frac{-(t-(\mu_1+\mu_2)^2}{2(\sigma_1+\sigma_2)^2}}}{(\sigma_1+\sigma_2)\sqrt{2\pi}} \tag{A.13}$$

Therefore the standard deviation σ_s adds up as follows

$$\sigma_s = \sqrt{\sigma_1^2 + \sigma_2^2}. \tag{A.14}$$

A.4 Transmission spectra

All transmission spectra were taken with a Perkin Elmer Lambda 950 UV/VIS Spectrometer.

A.4.1 IF filter I

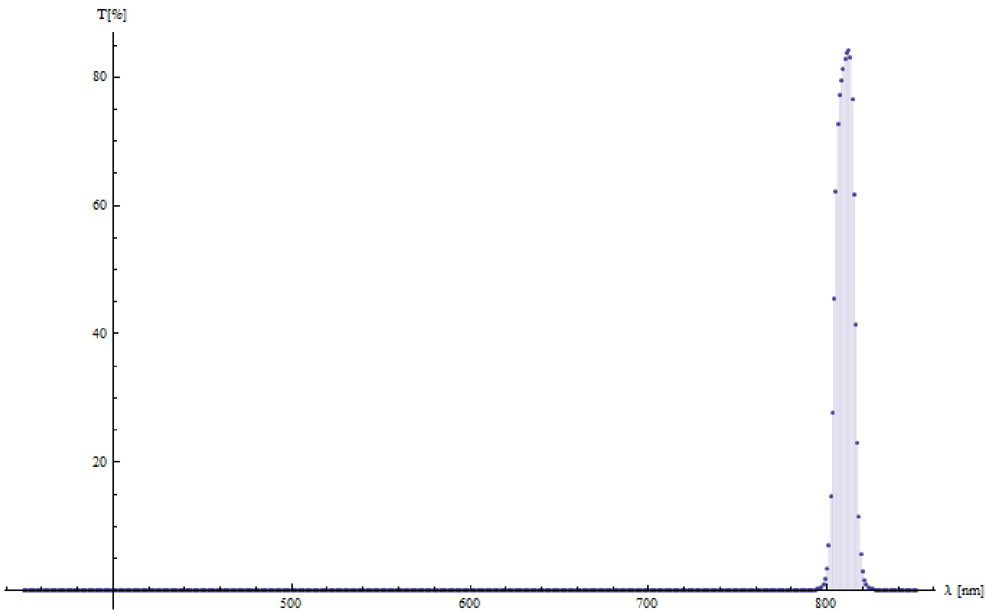

FIGURE A.2: Transmission spectrum of the 10nm IF filter with a colored glass filter from 350nm to 835nm.

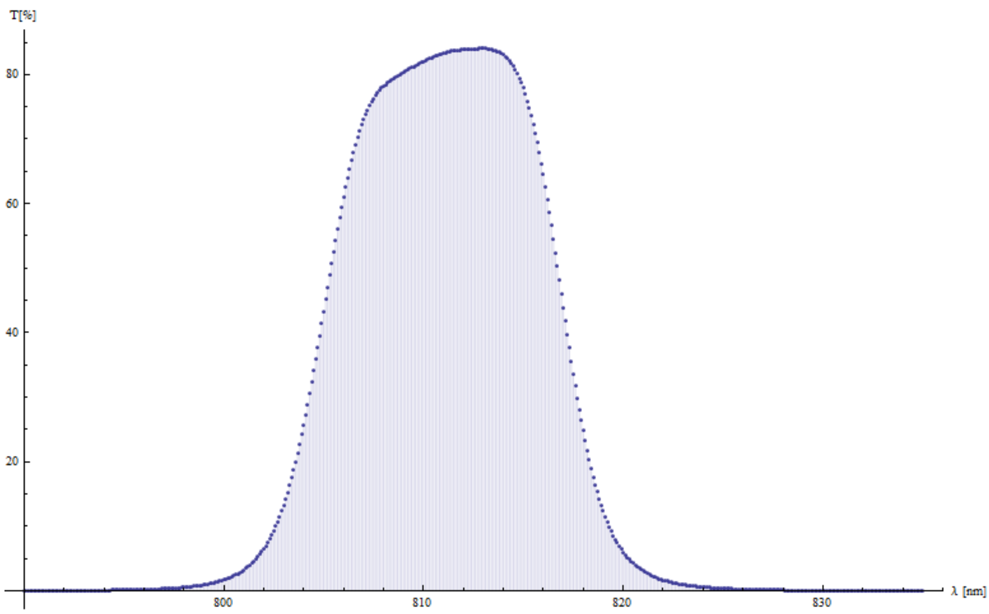

FIGURE A.3: Transmission spectrum of the 10nm IF filter with a colored glass filter from 790nm to 835nm.

A.4.2 IF filter II

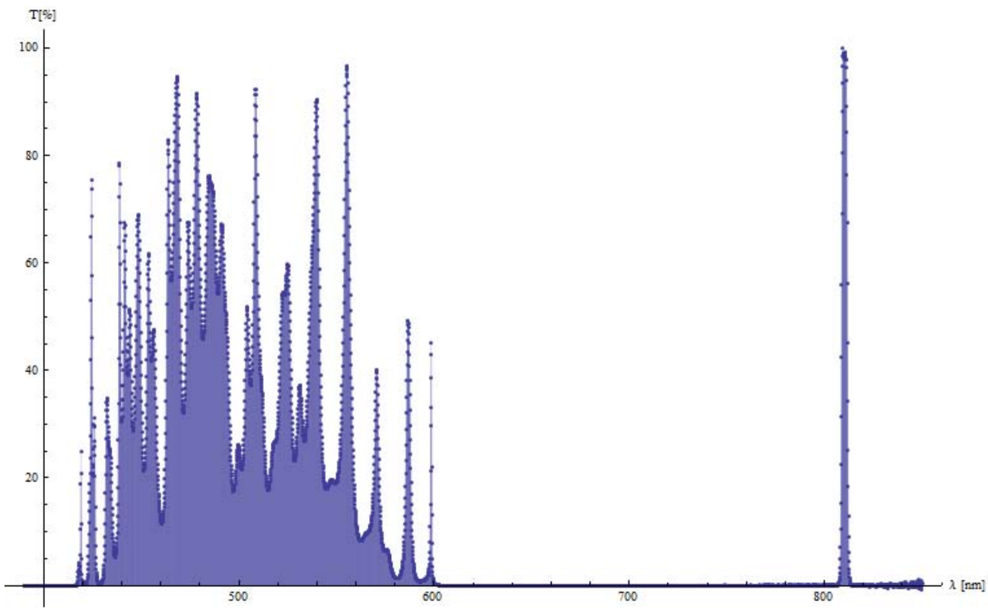

Figure A.4: Transmission spectrum of the 3nm Semrock IF filter from 400nm to 835nm.

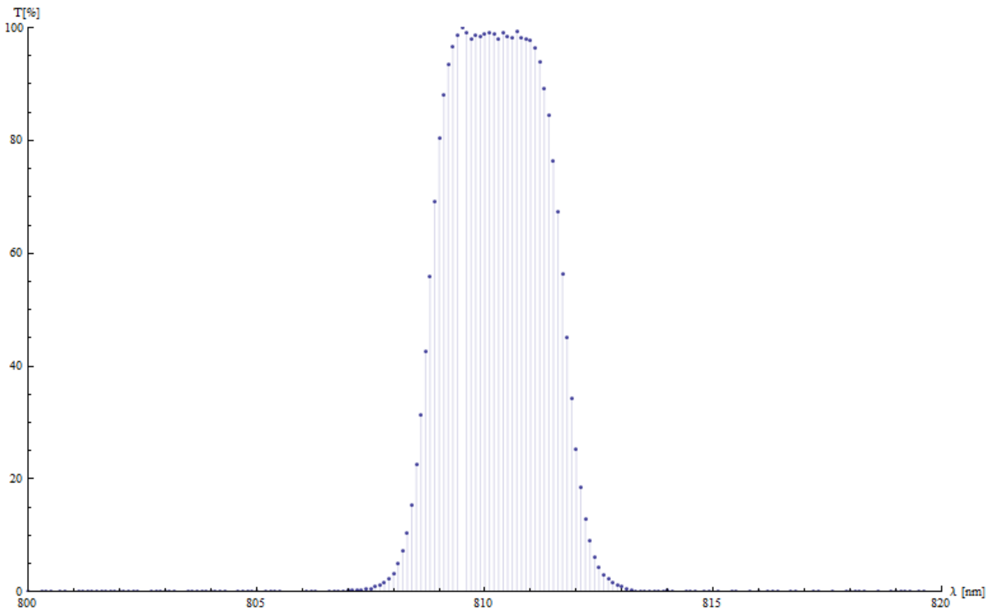

Figure A.5: Transmission spectrum of the 3nm Semrock IF filter from 800nm to 820nm.

A.4.3 Colored glass filter

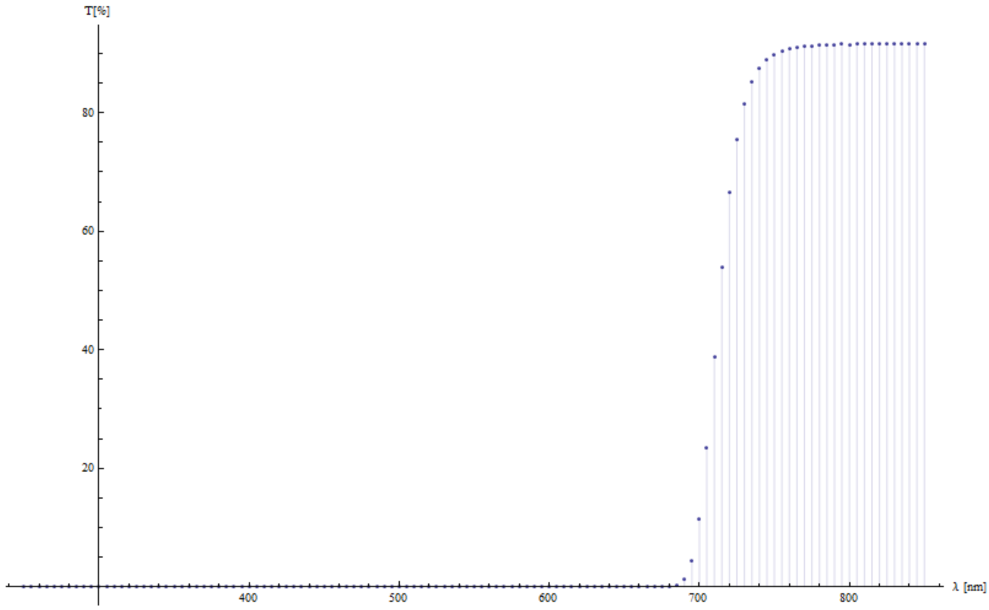

FIGURE A.6: Transmission spectrum of the colored glass filter from 300nm to 850nm.

A.4.4 Dichroic mirror

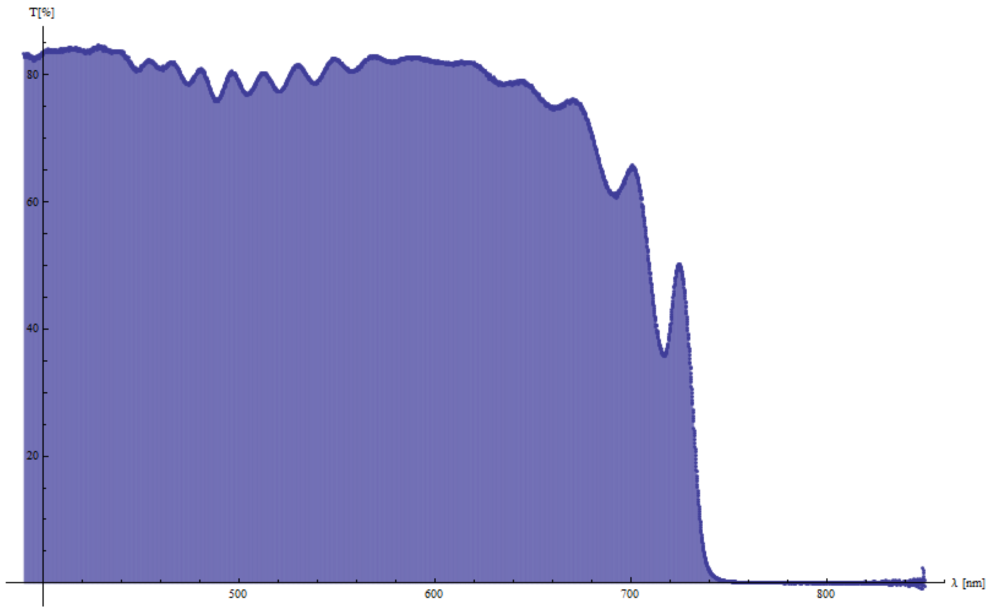

FIGURE A.7: Transmission spectrum from the dichroic mirror for separating the signal from the pump beam from 400nm to 850nm.

Appendix B

Sellmaier equations

Potassium titanyl phosphate:

$$
\begin{aligned}
n_y &= \sqrt{2.19229 + \frac{0.83547}{1 - 0.04970\lambda^2} - 0.01621 \cdot \lambda^2} \\
n_z &= \sqrt{2.25411 + \frac{1.06543}{1 - 0.05486\lambda^2} - 0.02140 \cdot \lambda^2}
\end{aligned}
\tag{B.1}
$$

Fused silica:

$$
\begin{aligned}
n_x &= \sqrt{1 + \frac{0.6961663 \cdot \lambda^2}{\lambda^2 - 4.67914826 \cdot 10^{-3}} + \frac{0.407942600 \cdot \lambda^2}{\lambda^2 - 1.35120631 \cdot 10^{-2}} + \frac{0.897479400 \cdot \lambda^2}{\lambda^2 - 97.9340025}} \\
n_y &= \sqrt{1 + \frac{0.6961663 \cdot \lambda^2}{\lambda^2 - 4.67914826 \cdot 10^{-3}} + \frac{0.407942600 \cdot \lambda^2}{\lambda^2 - 1.35120631 \cdot 10^{-2}} + \frac{0.897479400 \cdot \lambda^2}{\lambda^2 - 97.9340025}}
\end{aligned}
\tag{B.2}
$$

Bariumborat:

$$
\begin{aligned}
n_y &= \sqrt{2.7359 + \frac{0.01878}{\lambda^2 - 0.01822} - 0.01354 \cdot \lambda^2} \\
n_z &= \sqrt{2.3753 + \frac{0.01224}{\lambda^2 - 0.01667} - 0.01516 \cdot \lambda^2}
\end{aligned}
\tag{B.3}
$$

Quartz:

$$
\begin{aligned}
n_x &= \sqrt{2.35728 - 0.0117 \cdot \lambda^2 + \frac{0.01054}{\lambda^2} + \frac{0.000134143}{\lambda^4} - \frac{0.0000000445368}{\lambda^6} + \frac{0.0000000592362}{\lambda^8}} \\
n_y &= \sqrt{2.3849 - 0.01259 \cdot \lambda^2 + \frac{0.01079}{\lambda^2} + \frac{0.00016518}{\lambda^4} - \frac{0.000000194741}{\lambda^6} + \frac{0.0000000592362}{\lambda^8}}
\end{aligned}
\tag{B.4}
$$

Calcite:

$$\begin{aligned} n_y &= \sqrt{2.69705 + \frac{0.0192064}{\lambda^2 - 0.01820} - 0.0151624 \cdot \lambda^2} \\ n_z &= \sqrt{2.18438 + \frac{0.0087309}{\lambda^2 - 0.01018} - 0.0024411 \cdot \lambda^2} \end{aligned} \tag{B.5}$$

Yttrium orthovanadate:

$$\begin{aligned} n_y &= \sqrt{3.77834 + \frac{0.069736}{\lambda^2 - 0.04724} - 0.0108133 \cdot \lambda^2} \\ n_z &= \sqrt{4.59905 + \frac{0.110534}{\lambda^2 - 0.048138} - 0.012267612 \cdot \lambda^2} \end{aligned} \tag{B.6}$$

Magnesium flouride:

$$\begin{aligned} n_y &= \sqrt{1 + \frac{0.487551086 \cdot \lambda^2}{\lambda^2 - 0.04338408^2} + \frac{0.39875031 \cdot \lambda^2}{\lambda^2 - 0.09461442^2} + \frac{2.3120353 \cdot \lambda^2}{\lambda^2 - 23.793604^2}} \\ n_z &= \sqrt{1 + \frac{0.41344023 \cdot \lambda^2}{\lambda^2 - 0.03684262^2} + \frac{0.50497499 \cdot \lambda^2}{\lambda^2 - 0.09076162^2} + \frac{2.4904862 \cdot \lambda^2}{\lambda^2 - 23.793604^2}} \end{aligned} \tag{B.7}$$

Appendix C

Datasheets

C.1 PM-fibre

Polarization Maintaining Short Wavelength Fibers

Nufern's industry leading visible and short wavelength Polarization Maintaining fibers have superior waveguide, radiation, and mechanical properties enabling a large variety of new critical applications in diverse markets. High consistency and extreme end-to-end control of optical properties provide particular advantage in spectrographic and frequency sensitive applications. The intrinsically high level of radiation resistance allows this family to operate for extended periods of time on low earth orbits, near and deep space, and in applications where risk of exposure to man-made radiation is great.

Typical Applications

- Laser pigtailing
- Spectroscopy
- Sensors
- Bio-medical
- Metrology

Features & Benefits

- Panda-style configuration — Superior performance, intrinsically good radiation performance
- Tight specifications — Highly deterministic results, highest product yield
- High Proof Test — Low risk of mechanical handling failure
- High fatigue resistance — Longest service life

Optical Specifications	PM460-HP	PM630-HP	PM780-HP
Operating Wavelength	460 – 700 nm	620 – 850 nm	770 – 1100 nm
Core NA	0.120	0.120	0.120
Mode Field Diameter (Gaussian)	3.3 ± 0.5 µm @ 515 nm	4.5 ± 0.5 µm @ 630 nm	5.3 ± 1.0 µm @ 850 nm
Cutoff	410 ± 40 nm	570 ± 50 nm	710 ± 60 nm
Core Attenuation	≤ 100.0 dB/km @ 488 nm	≤ 15.0 dB/km @ 630 nm	≤ 4.0 dB/km @ 850 nm
Beat Length (nominal)	1.3 mm @ 460 nm	1.8 mm @ 630 nm	2.4 mm @ 850 nm
Normalized Cross Talk	N/A	N/A	≤ - 40 dB at 4 m @ 850 nm
Birefringence	nominal 3.5×10^{-4}	nominal 3.5×10^{-4}	nominal 3.5×10^{-4}
Geometrical & Mechanical Specifications			
Cladding Diameter	125.0 ± 1.0 µm	125.0 ± 1.0 µm	125.0 ± 1.0 µm
Core Diameter	3.0 µm	3.5 µm	4.5 µm
Coating Diameter	245.0 ± 15.0 µm	245.0 ± 15.0 µm	245.0 ± 15.0 µm
Coating Concentricity	< 5.0 µm	< 5.0 µm	< 5.0 µm
Core/Clad Offset	≤ 0.50 µm	≤ 0.50 µm	≤ 0.50 µm
Coating Material	UV Cured, Dual Acrylate	UV Cured, Dual Acrylate	UV Cured, Dual Acrylate
Operating Temperature Range	-40 to 85 °C	-40 to 85 °C	-40 to 85 °C
Prooftest Level	≥ 200 kpsi (1.4 GN/m²)	≥ 200 kpsi (1.4 GN/m²)	≥ 200 kpsi (1.4 GN/m²)

7 Airport Park Road, East Granby, CT 06026 • 860.408.5000 • Toll-free 866.466.0214 • Fax 860.844.0210 E-mail info @ nufern.com • www.nufern.com •
Nufern products are manufactured under an ISO 9001:2008 certified quality management system.

Standard specifications and design parameters are listed above. Specifications are subject to change without notice. Other configurations such as alternative form factors, optimized cut-off and UV cured color coating may be available. Let us know how Nufern can assist with your requirements.

C.2 Ondax laser

ONDAX

SureLock™

LM Series
Compact Single Frequency Laser Modules

Single Frequency

Ondax's LM Series Compact Single Frequency Laser Module incorporates the Ondax SureLock™ VHG-stabilized laser diode to deliver steady, single frequency performance in an ultra-compact footprint. Offering both computer and integrated user controls, the LM Series includes precision temperature and current controls to deliver better than 1m coherence length and 1% power stability with less than 1 minute warm-up. This tightly integrated package makes it the ideal choice for both OEM instrumentation and laboratory applications.

The LM Module is available in wavelengths from 405nm to 830nm.

Features:

- Single frequency, collimated TEM output with long coherence length (~1m)
- Remote computer and onboard user controls with integral LCD Display
- Precision temperature and current stabilization
- Ultra-compact footprint 40mm x 42.5mm x 100mm
- Plug and play operation
- NoiseBlock™narrow-band ASE suppression filters and beamsplitters available in matching wavelengths to further reduce linewidth and ASE noise

Applications:

- Raman Spectroscopy
- Interfereometry
- Metrology
- HeNe replacement
- Bio-instrumentation
- Particle Counting
- LIDAR
- Graphic Arts
- Sensing
- Analytical Instrumentation

Specifications:

Parameter	Sym-	Wavelength									
Center Wavelength (vaccuum)[1]	L_p/nm	405/406	633	638	658	685	690	780.25	785	808	830
Center Wavelength Tolerances	nm	±1	±0.5	±1	±1	±1	±1	±0.2	±1	±1	±1
Output Power	P_o/mW	12/25/40	40/75	30	30	40	40	75	75/100	150	200
Beam Size	mm	0.6 x 0.3	0.6 x 0.9	0.6 x 0.8	0.7 x 1.1	0.9 x 1.4	0.9 x 1.5	0.8 x 1.5	0.9 x 1.7	0.9 x 1.7	0.9 x 1.4
Linewidth, maximum (MHz)	$\Delta\lambda$	160[2]	150	300	300	50	100	50	50	50	250

[1]Available in increments of 2nm. Please specify wavelength at time of ordering. [2]For 405nm diode only

Operating Specifications

Optical	Min	Typ	Max	Unit
Spatial Mode			Single Mode	
Polarization		100:1		
Beam Divergence		1	10	mrad
Pointing Stability			± 25	µrad
Noise (RMS, 0-20 MHz)		0.25	0.5	%
Power Stability (1 hr)		0.10	0.5	%
Electrical	**Min**	**Typ**	**Max**	**Unit**
Operating Current			1.5	A
Operating Voltage		3.3		VDC
Modulation Input (TTL)	0		5	VDC
Modulation Speed			3	kHz
Environmental	**Min**	**Typ**	**Max**	**Unit**
Storage Temperature	-10		60	°C
Operating Temperature	10	25	40	°C
Operation Humidity			Non-condensing	
Dimensions (D x L)		100 x 80		mm

SureLock™

LM Series Compact Single Frequency Laser Modules

Wavelength Stability (405nm example)

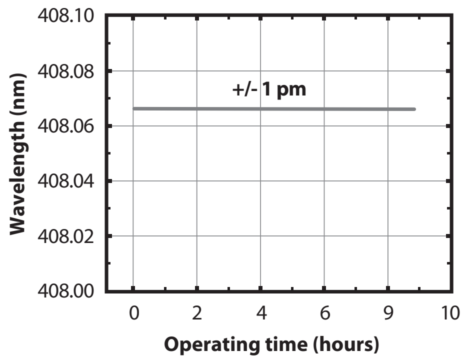

Optical Power Stability (405nm example)

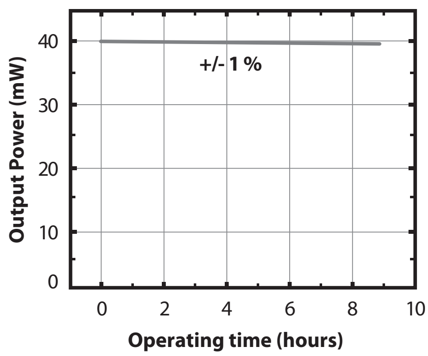

Optical Spectrum (405nm example)

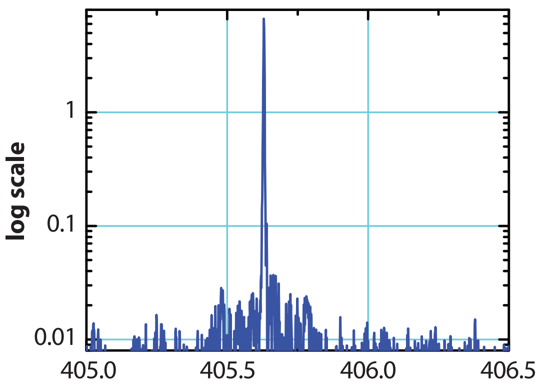

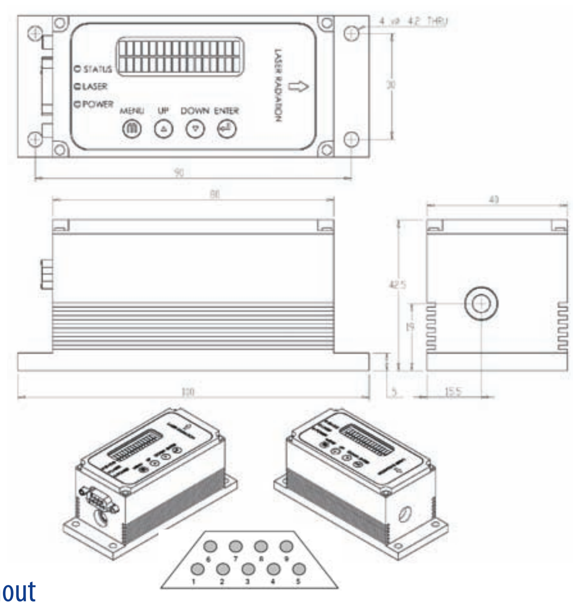

Model Numbers

LM-λλλ-PLR-Power or LM-λλλ-PLR-Power-1K (includes keyswitch)

Power Requirements

100-240V AC, 50-60Hz, Connector: +3.3VDC, 2.1mm dia.

Pinout

Pin	Definition	Description
1	VCC	Positive Power Pin +3.3V
2	TXD	Send data to computer (RS232)
3	RXD	Receive data from computer (RS232)
4		Not used
5	GND	GND for power and RS232 communication
6	TTL	Outside TTL modulation
7		Not used
8		Not used
9	GND	GND for power and RS232 communication

Note: Pinout is compatible with standard RS232 cable for interfacing with computer port or USB-RS232 adapter

ONDAX

850 E. Duarte Rd. Monrovia, CA 91016
626-357-9600 (Tel)
626-513-7494 (Sales Fax)

For more information about Ondax products and the name of a local representative or distributor, visit www.ondax.com, email sales@ondax.com, or call (626) 357-9600. Specifications subject to change without notice. Each purchased laser is provided with test data and manual. Please refer to this data before using the laser.

Bibliography

[1] CH Bennett and G Brassard. Quantum cryptography: Public key distribution and coin tossing. *Proceedings of IEEE International Conference on Computers, Systems and Signal Processing*, 175, 1984.

[2] Herbst. Entanglement-based quantum communication over long-distance free-space link. Master's thesis, Vienna UT, 2008.

[3] W. K. Wootters and W. H. Zurek. A single quantum cannot be cloned. *Nature*, 299:802–803, October 1982.

[4] C Simon, G Weihs, and A Zeilinger. Optimal Quantum Cloning Via Stimulated Emission. *Physical Review Letters*, 84:2993–2996, 2000.

[5] A Einstein, B Podolsky, and N Rosen. Can quantum-mechanical description of physical reality be considered complete? *Phys. Rev.*, 47:777–780, 1935. URL http://prola.aps.org/abstract/PR/v47/i10/p777_1.

[6] D Bohm and Y Aharonov. Discussion of Experimental Proof for the Paradox of Einstein, Rosen, and Podolsky. *Phys. Rev.*, 108(4):1070–1076, 1957. URL http://prola.aps.org/abstract/PR/v108/i4/p1070_1.

[7] John S Bell. On the Einstein Podolsky Rosen Paradox. *Physics*, 1:195, 1964.

[8] J F Clauser, M A Horne, A Shimony, and R A Holt. Proposed Experiment to Test Local Hidden-Variable Theories. *Physical Review Letters*, 23(15):880–884, January 1969. URL http://link.aps.org/doi/10.1103/PhysRevLett.23.880.

[9] Mehrdad S. Sharbaf. Quantum cryptography: An emerging technology in network security. *Technologies for Homeland Security (HST), 2011 IEEE International Conference on*, 2011.

[10] P W Shor and J Preskill. Simple Proof of Security of the BB84 Quantum Key Distribution Protocol. *Physical Review Letters*, 85(2):441–444, January 2000.

[11] A Poppe, A Fedrizzi, T Loruenser, O Maurhardt, R Ursin, H R Boehm, M Peev, M Suda, Ch Kurtsiefer, H Weinfurterand T Jennewein, and A Zeilinger. Practical Quantum Key Distribution with Polarization-Entangled Photons. *Opt. Express*, 12: 3865–3871, 2004.

[12] Morton H Rubin, David N Klyshko, Y H Shih, and A V Sergienko. Theory of two-photon entanglement in type-II optical parametric down-conversion. *Physical Review A*, 50(6):5122–5133, 1994.

[13] R W Boyd. *Nonlinear Optics*. Academic Press, 1992.

[14] Veronika Stelmakh. High-quality source of fiber-coupled polarization-entangled photons at 1.56μm. Master's thesis, Massachusetts Institute of Technology, 2012.

[15] Dieter H .Jundt Robert L. Byer Martin M. Fejer, G. A. Magel. Quasi-phase-matched second harmonic generation: tuning and tolerances. *Quantum Electronics, IEEE Journal of (Volume:28 , Issue: 11)*, 1992.

[16] Avalanche-photodiode. *Wikipedia*, 2014. URL http://de.wikipedia.org/wiki/Avalanche-Photodiode.

[17] Silicon avalanche photodiodes c30902 series high speed apds for analytical and biomedical lowest light detection applications. Data sheet, 2008. URL www.optoelectronics.perkinelmer.com.

[18] Marc Jofre Thomas Scheidl Juan P. Torres Valerio Pruneri Fabian Steinlechner, Marta Gilaberte and Rupert Ursin. Polarization-entangled photons from type-0 and type-ii spontaneous parametric down-conversion in a polarization sagnac interferometer. *in preparation*, 2014.

[19] Paul G. Kwiat, Klaus Mattle, Harald Weinfurter, Anton Zeilinger, Alexander V Sergienko, and Yanhua Shih. New High-Intensity Source of Polarization-Entangled Photon Pairs. *Physical Review Letters*, 75(24):4337–4342, 1995.

[20] S.Leveque N.Schuhler. Characterization of the performance of ppktp for the second harmonic generation of a 1319nm nd-yag laser. Technical Report VLT-TRE-ESO-15731-3065, EUROPEAN SOUTHERN OBSERVATORY, August 2003.

[21] A Fedrizzi. *Fundamental experiments with a high brightness source of entangled photons*. PhD thesis, University of Vienna, 2008.

[22] Dr. Ruediger Paschotta. *Polarization-maintaining Fibers http://www.rp-photonics.com/polarization_maintaining_fibers.html?s=ak (09.05.2014).*

[23] GREGOR WEIHS and ANTON ZEILINGER. Photon statistics at beam splitters: an essential tool in quantum information and teleportation.

[24] *Manual Fiber Polarization Controllers* *http://www.thorlabs.de/newgrouppage9.cfm?objectgroup_id=343* *(09.05.2014).*

[25] Matthias Fink. Development of a receiver module for optical free space quantum key distribution. Master's thesis, Vienna UT, 2014.

[26] *TTM8000 Time Tagging Module with 8-Channels.* Austrian Institue of Technology, 4.3.1 edition, 11 2013.

Acknowledgements

First and foremost, I dedicate this work to my parents Hermine and Ernst for the best support since I am able to remember.

I am grateful to Prof. Anton Zeilinger from the IQOQI offering me the opportunity to work in such an inspiring place for a physicist. I also want to thank Dr. Rupert Ursin, Dr. Thomas Scheidl and DI Thomas Herbst for the awesome time and for sharing their knowledge with me. I want to thank Matthias Fink for the best accompany during this one and a half year of time intense work and I would like to thank all the involved people on the institute for the fruitful discussions and fun as well.

This work was made possible by grants from the Federal Ministry of Science, Research and Economy(BMWFW) under project QUESS MM725002 and the Austrian Science Foundation(FWF) under project SFB F4008.

Last but not least I also want to thank my beloved siblings and my close friends, despite working in this mind blowing field of physics, for keeping me grounded.

DANKE!